

# Application of the Complex Image Method to Electromagnetic Field Computation in Planar Uniaxial Multilayers

Krzysztof Arkadiusz Michalski

Department of Electrical and Computer Engineering  
Texas A&M University  
College Station, Texas 77843, USA  
`krys@ece.tamu.edu`

June 11, 2015

## Abstract

The discrete complex image method (DCIM) is applied to compute the complete set of electric, magnetic, and potential Green functions (or integral equation kernels) for planar multilayers with uniaxial anisotropy. It is assumed that the layered medium is of infinite lateral extent and the optic axis is normal to the stratification. Sample results are presented and are shown to be in good agreement with reference data obtained by a rigorous integration method.

*Keywords:* Discrete complex image method, Green function, integral equation, layered medium, uniaxial medium.

## 1 Introduction

In a variety of applications, such as the analysis of microstrip circuits and antennas or VLSI interconnects, it is necessary to compute the electromagnetic field due to time-harmonic currents embedded in planar multilayered media. It can often be assumed that the layered medium is of infinite lateral extent. Usually, integral equation methods, based on surface or volume formulations, are used in this context, because they only require the discretization of the scattering object, with the layered background rigorously incorporated via the appropriate (dyadic) Green functions. The Green functions (or integral equation kernels) in such environments give rise to *Sommerfeld integrals*, which are time-consuming to evaluate, due to the singular and oscillatory nature of the integrands [1, 2]. Consequently, “brute-force” numerical integration is not practical. To alleviate this problem, the discrete complex image method (DCIM) was developed [3, 4]. The key step of the DCIM is an approximation of the spectral integrand by a finite sum of complex exponential terms, which can be associated with discrete images of the source at complex-valued locations in an

“equivalent” homogeneous medium. The advantage of this method is that the image representation has a closed-form inverse.

A lot of effort has recently been directed at the development of robust DCIM representations of Green’s function in layered media [5–11]. However, with a few exceptions [6, 7], this effort was limited to the the vector and scalar potential kernels associated with the so-called mixed-potential integral equation (MPIE) [12–15], which are easier to handle than the more singular field kernels. Furthermore, with one exception known to us [16], previous work was limited to isotropic media, even though the MPIE formulation for uniaxial multilayers had been known for quite some time [15, 17]. In [16], results are only presented for the scalar potential kernel in a grounded-slab configuration.

In the present paper, we describe the application of the DCIM to the complete set of electric, magnetic, and MPIE kernels for multilayers that may comprise uniaxially anisotropic media with the optic axis normal to the stratification.

## 2 Problem statement

We consider a plane-stratified medium excited by arbitrary, time-harmonic,<sup>1</sup> electric and magnetic currents,  $\mathbf{J}$  and  $\mathbf{M}$ , respectively,<sup>2</sup> occupying a volume  $V$  or residing on a surface  $S$ , as illustrated in Fig. 1a. The stratification is perpendicular to the  $z$  axis and of infinite lateral extent along the  $x$  and  $y$  axes. The layers are numbered from 1 to  $N$  in the direction of increasing  $z$ , where the number of layers,  $N$ , is arbitrary. The  $n$ th layer, with interfaces at  $z = z_n$  and  $z = z_{n+1}$ , is filled with a homogeneous, linear, possibly lossy, possibly uniaxial medium, characterized by diagonal permittivity and permeability tensors

$$\underline{\underline{\epsilon}}_n = (\hat{x}\hat{x} + \hat{y}\hat{y})\epsilon_{tn} + \hat{z}\hat{z}\epsilon_{zn}, \quad (1)$$

$$\underline{\underline{\mu}}_n = (\hat{x}\hat{x} + \hat{y}\hat{y})\mu_{tn} + \hat{z}\hat{z}\mu_{zn}, \quad (2)$$

where  $\epsilon_{tn}$  and  $\epsilon_{zn}$  are transverse and longitudinal permittivities, and  $\mu_{tn}$  and  $\mu_{zn}$  are transverse and longitudinal permeabilities, all relative to free space.<sup>3</sup> The sources may occupy any number of layers, including the interfaces. The quantities of interest are the electric and magnetic fields,  $\mathbf{E}$  and  $\mathbf{H}$ , respectively, at an arbitrary location  $\mathbf{r}$ . In solving this problem, use will be made of the spectral domain transmission line analogue of the multilayer, illustrated in Fig. 1b, whose parameters will be defined in due course.

The multilayer may optionally be shielded below and/or above by impenetrable planes that present three possible boundary conditions: 1)  $\hat{\mathbf{n}} \times \mathbf{E} = Z_s \hat{\mathbf{n}} \times (\hat{\mathbf{n}} \times \mathbf{H})$ , where  $\hat{\mathbf{n}}$  is the interface normal vector and  $Z_s$  is a specified surface impedance, 2)  $\hat{\mathbf{n}} \times \mathbf{E} = 0$ , which defines a perfect electric conductor (PEC), and 3)  $\hat{\mathbf{n}} \times \mathbf{H} = 0$ , which defines a perfect magnetic conductor (PMC). If the multilayer stack is unshielded, virtual interfaces are placed at  $z_1$  and  $z_{N+1}$ , and all sources and field points are assumed to lie between or on these planes.

<sup>1</sup>The  $e^{j\omega t}$  time convention is used.

<sup>2</sup>Throughout this paper vectors are denoted by boldface letters, unit vectors are distinguished by carets, and dyadics (i.e., second-rank Cartesian tensors) are denoted by doubly underlined boldface letters.

<sup>3</sup>Note that optical axis of the medium is assumed to be normal to the stratification.

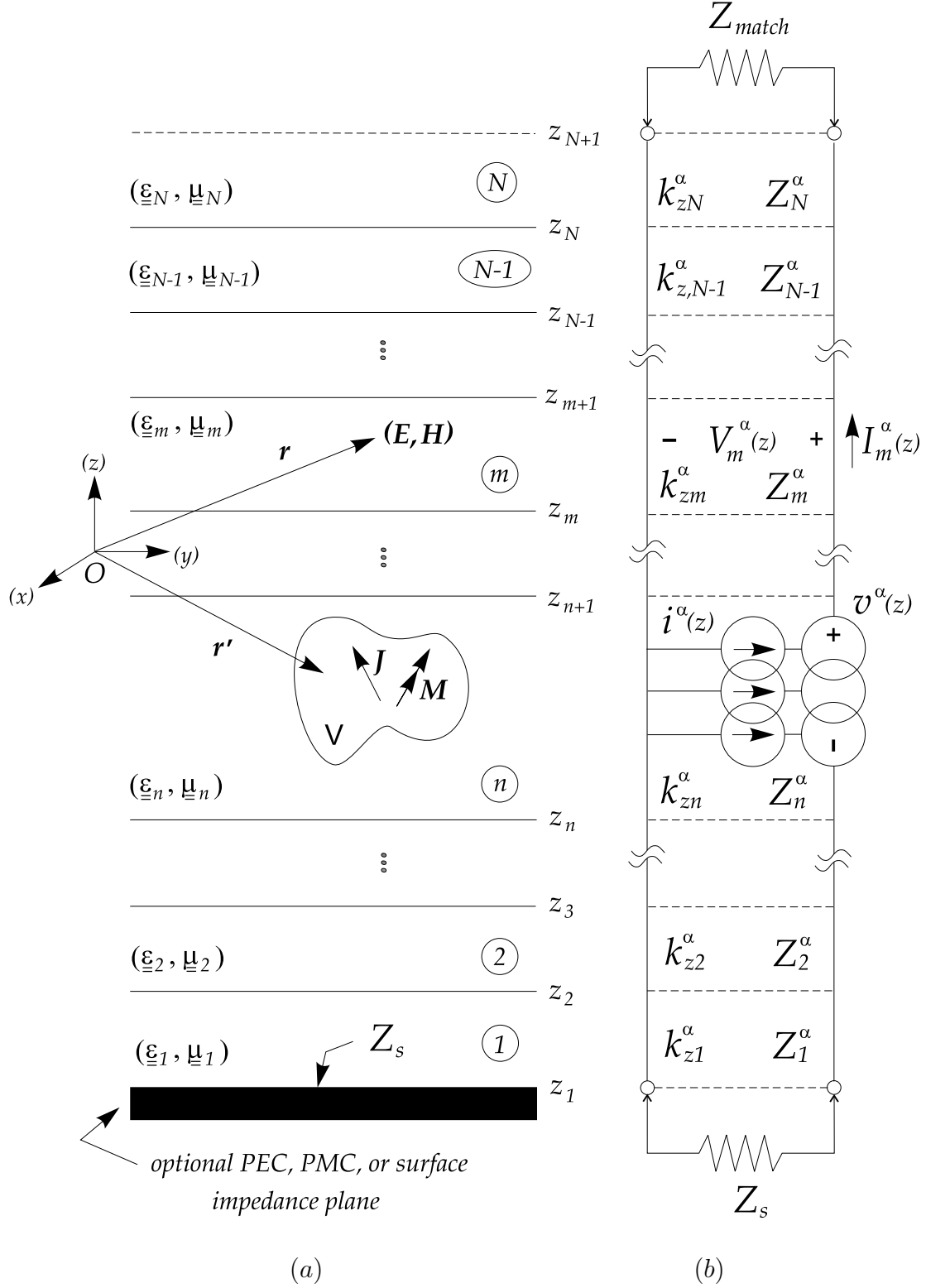


Figure 1: Electric and magnetic currents in a layered medium. (a) Physical configuration. (b) Spectral domain transmission-line equivalent circuit.

The electric and magnetic fields due to arbitrary electric and magnetic current distributions can be expressed in the form [15, 18]

$$\mathbf{E}(\mathbf{r}) = \langle \underline{\underline{\mathbf{G}}}^{EJ}(\mathbf{r}|\mathbf{r}'); \mathbf{J}(\mathbf{r}') \rangle + \langle \underline{\underline{\mathbf{G}}}^{EM}(\mathbf{r}|\mathbf{r}'); \mathbf{M}(\mathbf{r}') \rangle, \quad (3)$$

$$\mathbf{H}(\mathbf{r}) = \langle \underline{\underline{\mathbf{G}}}^{HM}(\mathbf{r}|\mathbf{r}'); \mathbf{M}(\mathbf{r}') \rangle + \langle \underline{\underline{\mathbf{G}}}^{HJ}(\mathbf{r}|\mathbf{r}'); \mathbf{J}(\mathbf{r}') \rangle, \quad (4)$$

where  $\underline{\underline{\mathbf{G}}}^{PQ}(\mathbf{r}|\mathbf{r}')$  is the dyadic Green function (or kernel) relating  $P$ -type fields at  $\mathbf{r}$  and  $Q$ -type currents at  $\mathbf{r}'$ .<sup>4</sup> As a consequence of the translational symmetry of the medium with respect to the transverse coordinates,

$$\underline{\underline{\mathbf{G}}}^{PQ}(\mathbf{r}|\mathbf{r}') \equiv \underline{\underline{\mathbf{G}}}^{PQ}(\boldsymbol{\rho} - \boldsymbol{\rho}'; z|z'), \quad (5)$$

where  $\boldsymbol{\rho}$  is the projection of  $\mathbf{r}$  on the  $xy$ -plane.<sup>5</sup> The dyadic kernels possess the reciprocity properties

$$\underline{\underline{\mathbf{G}}}^{EJ}(\mathbf{r}|\mathbf{r}') = [\underline{\underline{\mathbf{G}}}^{EJ}(\mathbf{r}'|\mathbf{r})]^T, \quad (6)$$

$$\underline{\underline{\mathbf{G}}}^{HM}(\mathbf{r}|\mathbf{r}') = [\underline{\underline{\mathbf{G}}}^{HM}(\mathbf{r}'|\mathbf{r})]^T, \quad (7)$$

$$\underline{\underline{\mathbf{G}}}^{HJ}(\mathbf{r}|\mathbf{r}') = -[\underline{\underline{\mathbf{G}}}^{EM}(\mathbf{r}'|\mathbf{r})]^T. \quad (8)$$

To simplify notation, we may also express (3)–(4) as<sup>6</sup>

$$\mathbf{E}[\mathbf{J}, \mathbf{M}] = \langle \underline{\underline{\mathbf{G}}}^{EJ}; \mathbf{J} \rangle + \langle \underline{\underline{\mathbf{G}}}^{EM}; \mathbf{M} \rangle, \quad (9)$$

$$\mathbf{H}[\mathbf{J}, \mathbf{M}] = \langle \underline{\underline{\mathbf{G}}}^{HM}; \mathbf{M} \rangle + \langle \underline{\underline{\mathbf{G}}}^{HJ}; \mathbf{J} \rangle. \quad (10)$$

Since the operators  $\mathbf{E}[\mathbf{J}, \mathbf{0}]$  and  $\mathbf{H}[\mathbf{0}, \mathbf{M}]$  comprise hyper-singular kernels, it is usually advantageous to express them in the *mixed-potential form*<sup>7</sup>

$$\mathbf{E}[\mathbf{J}, \mathbf{0}] = -j\omega \mathbf{A} - \nabla \Phi, \quad (11)$$

$$\mathbf{H}[\mathbf{0}, \mathbf{M}] = -j\omega \mathbf{F} - \nabla \Psi, \quad (12)$$

where

$$\mathbf{A} = \mu_0 \langle \underline{\underline{\mathbf{G}}}^A; \mathbf{J} \rangle, \quad (13)$$

$$\mathbf{F} = \epsilon_0 \langle \underline{\underline{\mathbf{G}}}^F; \mathbf{M} \rangle, \quad (14)$$

$$\Phi = \frac{1}{\epsilon_0} \langle G^\Phi, q \rangle, \quad (15)$$

$$\Psi = \frac{1}{\mu_0} \langle G^\Psi, m \rangle. \quad (16)$$

In the above,  $\mu_0$  and  $\epsilon_0$  denote the free-space permeability and permittivity,  $\mathbf{A}$  and  $\mathbf{F}$  are the magnetic and electric vector potentials,  $\Phi$  and  $\Psi$  are the electric and magnetic scalar potentials,

<sup>4</sup>The notation  $\langle \cdot, \cdot \rangle$  is used for integrals of products of two functions separated by the comma over their common spatial support, with a dot over the comma indicating a dot product. Source coordinates are distinguished by primes.

<sup>5</sup>Note that this property does not hold in laterally shielded environments.

<sup>6</sup>The dependence on  $\mathbf{r}$  and  $\mathbf{r}'$  will not be indicated when there is no danger of confusion.

<sup>7</sup>The “mixed-potential” designation was originally introduced to emphasize that the equations comprise both vector and scalar potentials [12].

and  $q$  and  $m$  are the electric and magnetic charge densities, respectively. The charge and current densities are related by the continuity equations

$$\nabla \cdot \mathbf{J} = -j\omega q, \quad \nabla \cdot \mathbf{M} = -j\omega m. \quad (17)$$

Written more explicitly, equations (11)–(12) become

$$\mathbf{E}[\mathbf{J}, \mathbf{0}] = -j\omega\mu_0 \langle \underline{\underline{\mathbf{G}}}^A; \mathbf{J} \rangle + \frac{1}{j\omega\epsilon_0} \nabla \langle G^\Phi, \nabla' \cdot \mathbf{J} \rangle, \quad (18)$$

$$\mathbf{H}[\mathbf{0}, \mathbf{M}] = -j\omega\epsilon_0 \langle \underline{\underline{\mathbf{G}}}^F; \mathbf{M} \rangle + \frac{1}{j\omega\mu_0} \nabla \langle G^\Psi, \nabla' \cdot \mathbf{M} \rangle, \quad (19)$$

where the primed operator nabla indicates differentiation with respect to the source coordinates.

The mixed-potential expressions are less singular than the field forms, because some of the derivatives are extracted from the kernels and transferred to the source functions. Furthermore, in integral equation solutions by the method of moments, *weak forms* of these equations are used, in which the gradient operators can be transferred to the test functions.<sup>8</sup> Hence, assuming that  $\mathbf{J}$  and  $\mathbf{M}$  are surface currents residing on a *smooth* surface  $S$ , we obtain the weak forms of (3)–(4) as

$$\begin{aligned} \langle \mathbf{\Lambda}; \mathbf{E} \rangle = & -j\omega\mu_0 \langle \mathbf{\Lambda}; \langle \underline{\underline{\mathbf{G}}}^A; \mathbf{J} \rangle \rangle + \frac{1}{j\omega\epsilon_0} \langle \nabla \cdot \mathbf{\Lambda}, \langle G^\Phi, \nabla' \cdot \mathbf{J} \rangle \rangle \\ & + \langle \mathbf{\Lambda}; \langle \underline{\underline{\mathbf{G}}}^{EM}; \mathbf{M} \rangle \rangle \pm \frac{1}{2} \langle \mathbf{\Lambda}; \hat{\mathbf{n}} \times \mathbf{M} \rangle, \end{aligned} \quad (20)$$

$$\begin{aligned} \langle \mathbf{\Lambda}; \mathbf{H} \rangle = & -j\omega\epsilon_0 \langle \mathbf{\Lambda}; \langle \underline{\underline{\mathbf{G}}}^F; \mathbf{M} \rangle \rangle + \frac{1}{j\omega\mu_0} \langle \nabla \cdot \mathbf{\Lambda}, \langle G^\Psi, \nabla' \cdot \mathbf{M} \rangle \rangle \\ & + \langle \mathbf{\Lambda}; \langle \underline{\underline{\mathbf{G}}}^{HJ}; \mathbf{J} \rangle \rangle \mp \frac{1}{2} \langle \mathbf{\Lambda}; \hat{\mathbf{n}} \times \mathbf{J} \rangle, \end{aligned} \quad (21)$$

where  $\hat{\mathbf{n}}$  is a unit vector normal to  $S$  and  $\mathbf{\Lambda}$  is a vector test function tangential to  $S$ . Here, the upper signs result if  $S$  is approached from the side into which the surface normal  $\hat{\mathbf{n}}$  points, and the lower signs result if  $S$  is approached from the opposite side [20]. The symbol  $\langle \cdot, \cdot \rangle$  indicates that the integral is evaluated in the principal value sense, i.e., it represents contributions from all points of  $S$ , *excluding* the isolated point  $\mathbf{r}' = \mathbf{r}$ . Similar weak forms can also be derived for sources distributed over a volume  $V$ , rather than surface  $S$ .

The purpose of this project is to devise and implement the most efficient method for the computation of the dyadic Green functions (kernels) that arise in the field and mixed-potential representations of the electromagnetic fields.

### 3 Spectral-domain transmission-line analogue

The layered medium problem of Fig. 1a has a transmission-line network analogue shown in Fig. 1b, which can be derived by a Fourier transformation of the Maxwell's equations with respect to the transverse coordinates [18]. The transverse spectral wavenumber will be denoted by  $k_\rho$ . In general, two transmission-line networks arise, one associated with transverse-magnetic (TM) waves, and

<sup>8</sup>The term “weak form” means that the equation is enforced in a weighted average sense [19].

one associated with transverse-electric (TE) waves. The quantities pertaining to these two networks will be distinguished by the superscripts  $e$  and  $h$ , respectively. Hence, the superscript  $\alpha$  in Fig. 1b and in what follows stands for either  $e$  or  $h$ . Each transmission-line section of these networks is characterized by the propagation constants

$$k_z^\alpha = \sqrt{k_0^2 n_t^2 - k_\rho^2 / \nu^\alpha} = \frac{1}{\lambda^\alpha} \sqrt{k_0^2 (n_{\text{eff}}^\alpha)^2 - k_\rho^2}, \quad (22)$$

and characteristic impedances

$$Z^e = \frac{\eta_0 k_z^e}{k_0 \epsilon_t}, \quad Z^h = \frac{\eta_0 k_0 \mu_t}{k_z^h}, \quad (23)$$

where

$$n_t = \sqrt{\epsilon_t \mu_t}, \quad n_{\text{eff}}^e = \sqrt{\epsilon_z \mu_t}, \quad n_{\text{eff}}^h = \sqrt{\epsilon_t \mu_z}, \quad (24)$$

and

$$\nu^e = \frac{\epsilon_z}{\epsilon_t}, \quad \nu^h = \frac{\mu_z}{\mu_t}, \quad \lambda^\alpha = \sqrt{\nu^\alpha}. \quad (25)$$

It is important to note that, unlike in isotropic media, the propagation constants of the TM and TE transmission-line networks are in general different when the media are uniaxial. Since the media can be lossy, we assume that

$$\epsilon_t = \epsilon'_t - j\epsilon''_t, \quad \epsilon'_t > 0, \quad \epsilon''_t \geq 0, \quad (26)$$

and similarly for  $\epsilon_z$ ,  $\mu_t$ , and  $\mu_z$ . When computing the square roots in (22)–(24), the branch with non-positive imaginary part is selected.<sup>9</sup> The anisotropy ratios  $\lambda^\alpha$  are assumed to be real-valued. The medium is positive-uniaxial (electrically or magnetically), if  $\lambda^\alpha > 1$ , and negative-uniaxial, if  $\lambda^\alpha < 1$ . All media-dependent parameters in (22)–(26) should carry the layer index subscript, which we have omitted for notational simplicity.

A transmission-line section with index  $n$ , comprising unit-strength voltage and current sources at  $z'$ , is illustrated in Fig. 2, where  $\vec{\Gamma}_n$  and  $\overleftarrow{\Gamma}_n$  are the voltage reflection coefficients looking out

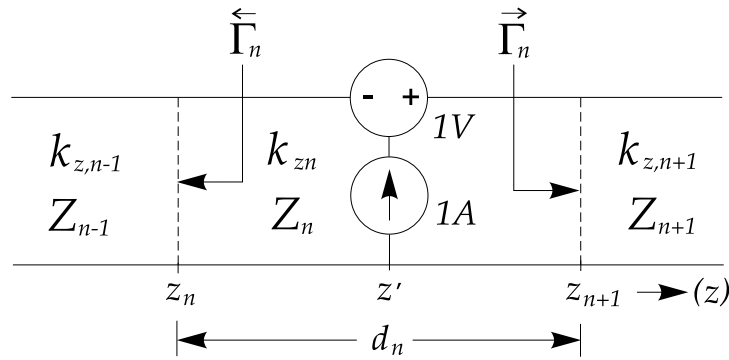


Figure 2: Voltage and current sources in a transmission line section.

<sup>9</sup>The intrinsic FORTRAN square root selects the branch with positive real part; if the real part is zero, it selects the root with positive imaginary part.

of the left and right terminals, respectively.<sup>10</sup> The left-looking (or down-looking) reflection coefficients are given by the recurrence relation [18]

$$\overleftarrow{\Gamma}_{n+1} = \frac{\Gamma_{n,n+1} + \overleftarrow{\Gamma}_n e^{-j2\theta_n}}{1 + \Gamma_{n,n+1} \overleftarrow{\Gamma}_n e^{-j2\theta_n}}, \quad (27)$$

where

$$\theta_n = k_{zn} d_n \quad (28)$$

and

$$\Gamma_{i,j} = \frac{Z_i - Z_j}{Z_i + Z_j} \quad (29)$$

is the Fresnel reflection coefficient across an interface between two half-spaces filled with media  $i$  and  $j$ , looking from medium  $j$ . The recursion (27) is applied beginning with the leftmost transmission-line section and proceeds forwards, section by section, toward the right end. The starting value,  $\overleftarrow{\Gamma}_1$ , is easily found. For example, if the first layer is of infinite extent, then it is reflectionless (the transmission line section is terminated by a matched load impedance), and the starting value is  $\overleftarrow{\Gamma}_1 = 0$ . If the first layer is backed by a plate with surface impedance  $Z_s$ , as illustrated in Fig. 1, then

$$\overleftarrow{\Gamma}_1 = \frac{Z_s - Z_1}{Z_s + Z_1}, \quad (30)$$

which becomes  $-1$  if the plate is PEC, and  $+1$  if it is PMC. For a good, but not perfect electrical conductor of conductivity  $\sigma$ ,  $Z_s$  can be found as

$$Z_s = \frac{1+j}{\sigma\delta}, \quad \delta = \sqrt{\frac{2}{\omega\mu_0\sigma}}, \quad (31)$$

where  $\delta$  is the skin depth. The right-looking (or up-looking) reflection coefficients satisfy the recurrence relation

$$\overrightarrow{\Gamma}_{n-1} = \frac{\Gamma_{n,n-1} + \overrightarrow{\Gamma}_n e^{-j2\theta_n}}{1 + \Gamma_{n,n-1} \overrightarrow{\Gamma}_n e^{-j2\theta_n}}, \quad (32)$$

which is applied beginning with the rightmost transmission-line section and proceeds backwards, toward the left end. The starting value,  $\overrightarrow{\Gamma}_N$ , is easily found, as explained in connection with the forward recursion.

We now introduce four basic transmission-line Green functions (TLGFs), as listed in Table 1.<sup>11</sup> It can be shown [21, p. 194] that these TLGFs possess the reciprocity properties<sup>12</sup>

$$V_i(z|z') = V_i(z'|z), \quad (33)$$

$$I_v(z|z') = I_v(z'|z), \quad (34)$$

$$V_v(z|z') = -I_i(z'|z). \quad (35)$$

<sup>10</sup>Since this figure and the following discussion pertain to both the TM and TE transmission-line networks, we omit the superscript  $\alpha$  for simplicity.

<sup>11</sup>For simplicity, we do not explicitly indicate the dependence of TLGFs on the transverse spectral wavenumber  $k_\rho$ .

<sup>12</sup>These relationships are intimately related to the reciprocity properties of the dyadic kernels given in (6)–(8).

Table 1: Definition of four transmission-line Green functions (TLGFs).

TLGF #	Notation	Definition
1	$V_i(z z')$	<i>voltage</i> at $z$ due to unit-strength <i>current</i> source at $z'$
2	$I_v(z z')$	<i>current</i> at $z$ due to unit-strength <i>voltage</i> source at $z'$
3	$I_i(z z')$	<i>current</i> at $z$ due to unit-strength <i>current</i> source at $z'$
4	$V_v(z z')$	<i>voltage</i> at $z$ due to unit-strength <i>voltage</i> source at $z'$

Explicit expressions for the TLGFs can readily be derived from their governing differential equations [18]. In particular, assuming that  $z$  and  $z'$  lie within the same line section  $n$ , and the source is of the current type, it is found that

$$V_i(z|z') = \frac{Z_n}{2} \left[ e^{-jk_{zn}|z-z'|} + \frac{1}{D_n} \sum_{s=1}^4 R_n^{(s)} e^{-jk_{zn}\zeta_n^{(s)}} \right], \quad (36)$$

$$I_i(z|z') = \frac{1}{2} \left[ \pm e^{-jk_{zn}|z-z'|} - \frac{1}{D_n} \sum_{s=1}^4 (-1)^s R_n^{(s)} e^{-jk_{zn}\zeta_n^{(s)}} \right], \quad (37)$$

where the  $\pm$  signs correspond to  $z \gtrless z'$ , and where

$$D_n = 1 - \overleftarrow{\Gamma}_n \overrightarrow{\Gamma}_n e^{-j2\theta_n} \quad (38)$$

is the *resonant denominator* and

$$R_n^{(1)} = \overleftarrow{\Gamma}_n, \quad R_n^{(2)} = \overrightarrow{\Gamma}_n, \quad R_n^{(3)} = R_n^{(4)} = \overleftarrow{\Gamma}_n \overrightarrow{\Gamma}_n, \quad (39)$$

$$\begin{aligned} \zeta_n^{(1)} &= (z + z') - 2z_n, & \zeta_n^{(2)} &= 2z_{n+1} - (z + z'), \\ \zeta_n^{(3)} &= 2d_n + (z - z'), & \zeta_n^{(4)} &= 2d_n - (z - z'). \end{aligned} \quad (40)$$

When the inverse resonant denominator is expanded in a geometric series as,

$$\frac{1}{D_n} = \sum_{m=0}^{\infty} \left( \overleftarrow{\Gamma}_n \overrightarrow{\Gamma}_n \right)^m e^{-j2m\theta_n}, \quad (41)$$

the expressions (36)–(37) may be given a geometric-optical ray interpretation, as illustrated in Fig. 3, where ray 0 represents the *direct term* and rays 1 through 4 represent four categories of rays that undergo partial reflections at the upper and lower layer boundaries before reaching the observation point [18]. It should be noted that the rays are strictly one-dimensional; the two-dimensional depiction is for convenience of visualization only. Although we do not use the ray forms to compute the TLGFs, the ray interpretation will become useful when we discuss the quasi-static image extraction in a later section.



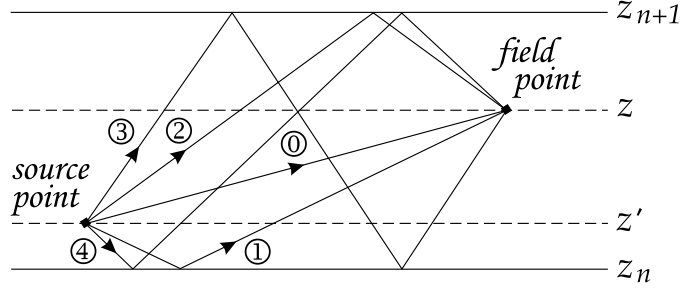


Figure 3: Ray interpretation of the TLGFs when  $z$  and  $z'$  are in the same layer  $n$ .

When  $z'$  is in section  $n$  and  $z$  is in section  $m > n$ , we introduce the voltage transfer function between the right terminals of the source section and the left terminals of the observation section, given as [18]

$$\vec{T}_{nm} = \prod_{k=n+1}^{m-1} \vec{\tau}_k, \quad (42)$$

where

$$\vec{\tau}_k \equiv \frac{V_{k+1}}{V_k} = \frac{(1 + \vec{\Gamma}_k) e^{-j\theta_k}}{1 + \vec{\Gamma}_k e^{-j2\theta_k}} \quad (43)$$

is the right-looking voltage transmission coefficient across the  $k$ th section. Here, we use the notation  $V_k = V(z_k)$ . The voltage at  $z$  within the  $m$ th section can now be found as [18]

$$V_m(z) = V_{n+1} \vec{T}_{nm} e^{-jk_{zm}(z-z_m)} \left[ \frac{1 + \vec{\Gamma}_m e^{-j2k_{zm}(z_{m+1}-z)}}{1 + \vec{\Gamma}_m e^{-j2\theta_m}} \right]. \quad (44)$$

With  $V_{n+1}$  computed as  $V_i(z_{n+1}|z')$  using (36), the above expression represents the TLGF  $V_i(z|z')$  for  $m > n$ .

A dual expression to (44), obtained by replacing the voltages by currents and the reflection coefficients by their negatives in (42)–(44), gives  $I_m(z)$  in terms of  $I_{n+1}$ . With the latter computed as  $I_i(z_{n+1}|z')$  using (37), this expression represents the transmission-line Green function  $I_i(z|z')$  for  $m > n$ .

The remaining TLGFs,  $I_v$  and  $V_v$ , are dual to  $V_i$  and  $I_i$ , respectively, and can be derived by simply replacing in the latter the characteristic impedances by their reciprocals and the reflection coefficients by their negatives [18, 22].

We have thus obtained all four TLGFs for  $m \geq n$ . There is no need to derive formulas for the case  $m < n$ , as we can use the reciprocity properties (33)–(35) to swap the locations of  $z$  and  $z'$ .

It is important to note the large- $k_\rho$  asymptotic behavior of the TLGFs, because it determines the source-region singularities of the kernels in the space domain and it can affect the computation of the Sommerfeld integrals. Clearly, the worst case arises when  $z = z'$ , since otherwise the TLGFs decay exponentially. We summarize this worst-case behavior in Table 2.

The above formulation of the TLGFs, which is based on the reflection coefficient method (and closely related to the impedance method), has the advantage that all exponentials are non-growing, thus eliminating the danger of numerical overflows for large  $k_\rho$ . Other formulations, such as the

Table 2: Worst-case asymptotic TLGF behavior.

TLGF	Asymptotic behavior for $z = z'$
$V_i^e, I_v^h$	$\mathcal{O}(k_\rho)$
$V_v^e, I_i^h, V_v^h, I_i^e$	$\mathcal{O}(1)$
$V_i^h, I_v^e$	$\mathcal{O}(k_\rho^{-1})$

ABCD-matrix method, or the T-matrix method [18] are also possible and useful in some applications. For example, in the development of the closed-form representations of layered media Green functions, it is important to extract the pole singularities, which can be found as zeros of a source-free modal dispersion function of the multilayer. An important property of the matrix methods is that they lead to analytic, pole-free modal dispersion functions, which are amenable to the root finding techniques based on the Cauchy theorem [23, 24].

## 4 Dyadic Green functions (kernels)

The scalar potential kernel and the elements of the dyadic vector potential kernel in (18) can be expressed as<sup>13</sup>

$$-\frac{1}{j\omega\epsilon_0} G^\Phi(\boldsymbol{\rho}; z|z') = \eta_0 G_0(\rho; z|z'), \quad (45)$$

$$j\omega\mu_0 G_{xx}^A(\boldsymbol{\rho}; z|z') = j\omega\mu_0 G_{yy}^A(\boldsymbol{\rho}; z|z') = \eta_0 k_0^2 G_1(\rho; z|z'), \quad (46)$$

$$j\omega\mu_0 G_{zz}^A(\boldsymbol{\rho}; z|z') = \eta_0 k_0^2 G_2(\rho; z|z'), \quad (47)$$

$$j\omega\mu_0 \begin{Bmatrix} G_{zx}^A(\boldsymbol{\rho}; z|z') \\ G_{zy}^A(\boldsymbol{\rho}; z|z') \end{Bmatrix} = \begin{Bmatrix} -j \cos \varphi \\ -j \sin \varphi \end{Bmatrix} \eta_0 k_0^2 G_3(\rho; z|z'), \quad (48)$$

$$j\omega\mu_0 \begin{Bmatrix} G_{xz}^A(\boldsymbol{\rho}; z|z') \\ G_{yz}^A(\boldsymbol{\rho}; z|z') \end{Bmatrix} = \begin{Bmatrix} -j \cos \varphi \\ -j \sin \varphi \end{Bmatrix} \eta_0 k_0^2 G_4(\rho; z|z'). \quad (49)$$

The elements of the two field kernels in (9) can be written as

$$\begin{aligned} -G_{xx}^{EJ}(\boldsymbol{\rho}; z|z') &= \frac{\eta_0 k_0^2}{2} \left[ G_5(\rho; z|z') \pm \cos 2\varphi G_6(\rho; z|z') \right], \\ -G_{yy}^{EJ}(\boldsymbol{\rho}; z|z') & \end{aligned} \quad (50)$$

$$-G_{xy}^{EJ}(\boldsymbol{\rho}; z|z') = -G_{yx}^{EJ}(\boldsymbol{\rho}; z|z') = \frac{\eta_0 k_0^2}{2} \sin 2\varphi G_6(\rho; z|z'), \quad (51)$$

$$\begin{aligned} -G_{xz}^{EJ}(\boldsymbol{\rho}; z|z') &= \begin{Bmatrix} j \cos \varphi \\ j \sin \varphi \end{Bmatrix} \eta_0 k_0^2 G_7(\rho; z|z'), \\ -G_{yz}^{EJ}(\boldsymbol{\rho}; z|z') & \end{aligned} \quad (52)$$

<sup>13</sup>Only nonzero Cartesian components of the dyadic kernels are listed.

$$\begin{aligned} -G_{zx}^{EJ}(\boldsymbol{\rho}; z|z') &= \begin{Bmatrix} j \cos \varphi \\ j \sin \varphi \end{Bmatrix} \eta_0 k_0^2 G_8(\boldsymbol{\rho}; z|z'), \\ -G_{zy}^{EJ}(\boldsymbol{\rho}; z|z') &= \begin{Bmatrix} j \cos \varphi \\ j \sin \varphi \end{Bmatrix} \eta_0 k_0^2 G_8(\boldsymbol{\rho}; z|z'), \end{aligned} \quad (53)$$

$$-G_{zz}^{EJ}(\boldsymbol{\rho}; z|z') = \eta_0 k_0^2 G_9 + \frac{\eta_0}{j k_0 \epsilon_z} \delta(\boldsymbol{\rho}) \delta(z - z'), \quad (54)$$

$$\begin{aligned} -G_{xx}^{EM}(\boldsymbol{\rho}; z|z') &= \mp \frac{k_0^2}{2} \sin 2\varphi G_{11}(\boldsymbol{\rho}; z|z'), \\ -G_{yy}^{EM}(\boldsymbol{\rho}; z|z') &= \mp \frac{k_0^2}{2} \sin 2\varphi G_{11}(\boldsymbol{\rho}; z|z'), \end{aligned} \quad (55)$$

$$\begin{aligned} -G_{xy}^{EM}(\boldsymbol{\rho}; z|z') &= \frac{k_0^2}{2} \left[ \pm G_{12}(\boldsymbol{\rho}; z|z') + \cos 2\varphi G_{11}(\boldsymbol{\rho}; z|z') \right], \\ -G_{yx}^{EM}(\boldsymbol{\rho}; z|z') &= \frac{k_0^2}{2} \left[ \pm G_{12}(\boldsymbol{\rho}; z|z') + \cos 2\varphi G_{11}(\boldsymbol{\rho}; z|z') \right], \end{aligned} \quad (56)$$

$$\begin{aligned} -G_{xz}^{EM}(\boldsymbol{\rho}; z|z') &= \begin{Bmatrix} +j \sin \varphi \\ -j \cos \varphi \end{Bmatrix} k_0^2 G_{13}(\boldsymbol{\rho}; z|z'), \\ -G_{yz}^{EM}(\boldsymbol{\rho}; z|z') &= \begin{Bmatrix} +j \sin \varphi \\ -j \cos \varphi \end{Bmatrix} k_0^2 G_{13}(\boldsymbol{\rho}; z|z'), \end{aligned} \quad (57)$$

$$\begin{aligned} -G_{zx}^{EM}(\boldsymbol{\rho}; z|z') &= \begin{Bmatrix} -j \sin \varphi \\ +j \cos \varphi \end{Bmatrix} k_0^2 G_{14}(\boldsymbol{\rho}; z|z'), \\ -G_{zy}^{EM}(\boldsymbol{\rho}; z|z') &= \begin{Bmatrix} -j \sin \varphi \\ +j \cos \varphi \end{Bmatrix} k_0^2 G_{14}(\boldsymbol{\rho}; z|z'). \end{aligned} \quad (58)$$

In the above,  $k_0 = \omega \sqrt{\epsilon_0 \mu_0}$  and  $\eta_0 = \sqrt{\mu_0 / \epsilon_0}$  are the free-space wavenumber and intrinsic impedance, respectively, and  $G_i$  are *basic kernels*, which will be introduced in due course.

In view of the duality between (18) and (19), the potential kernels in (19) can be obtained from (45)–(49) by the substitutions  $\Phi \rightarrow \Psi$ ,  $A \rightarrow F$ ,  $\mu_0 \rightarrow \epsilon_0$ ,  $\epsilon_0 \rightarrow \mu_0$ , and by replacing the basic kernels by the corresponding *dual kernels*. Similarly, the expressions for the first field kernel in (10) can be obtained from (50)–(54) by the substitutions  $EJ \rightarrow HM$ ,  $\eta_0 \rightarrow 1/\eta_0$ , and by using the dual forms of the basic kernels. Finally, the second field kernel in (10) can be computed from (55)–(58) by using the reciprocity relationship (8).

The above expressions assume that the source point is on the  $z$  axis of the cylindrical coordinate system  $(\rho, \varphi, z)$ . In the general case,  $\boldsymbol{\rho} \rightarrow \boldsymbol{\rho} - \boldsymbol{\rho}'$ , which implies the substitutions

$$\rho \rightarrow \sqrt{(x - x')^2 + (y - y')^2}, \quad \varphi \rightarrow \arctan \left( \frac{y - y'}{x - x'} \right), \quad (59)$$

where the quadrant of the argument must be noted when the inverse tangent is evaluated.<sup>14</sup>

The basic kernels can be expressed as<sup>15</sup>

$$G_0(\boldsymbol{\rho}; z|z') = \mathfrak{S}_0 \left\{ \frac{(V_i^h - V_i^e)}{\eta_0 k_\rho^2} \right\} = \mathfrak{S}_0^1 \left\{ \frac{(V_i^h - V_i^e)}{\eta_0 (k_\rho/k_0)^2} \right\}, \quad (60)$$

$$G_1(\boldsymbol{\rho}; z|z') = \mathfrak{S}_0 \left\{ \frac{V_i^h}{\eta_0 k_0^2} \right\} = \mathfrak{S}_0^1 \left\{ \frac{V_i^h}{\eta_0} \right\}, \quad (61)$$

$$G_2(\boldsymbol{\rho}; z|z') = \mathfrak{S}_0 \left\{ \left( \frac{\mu_t}{\epsilon'_z} + \frac{\mu'_t}{\epsilon_z} \right) \frac{\eta_0 I_v^e}{k_0^2} + \mu_t \mu'_t \frac{\eta_0 (I_v^h - I_v^e)}{k_\rho^2} \right\} \quad (62)$$

$$= \mathfrak{S}_0^1 \left\{ \left( \frac{\mu_t}{\epsilon'_z} + \frac{\mu'_t}{\epsilon_z} \right) \eta_0 I_v^e + \mu_t \mu'_t \frac{\eta_0 (I_v^h - I_v^e)}{(k_\rho/k_0)^2} \right\}, \quad (63)$$

<sup>14</sup>The intrinsic FORTRAN function ATAN2 does this automatically and returns a result in the range  $(-\pi, \pi]$  [25, p. 178].

<sup>15</sup>Note that there is no kernel  $G_{10}$ .

$$G_3(\rho; z|z') = \mathfrak{S}_1 \left\{ \mu_t \frac{(I_i^h - I_i^e)}{k_0 k_\rho} \right\} = \mathfrak{S}_1^0 \{ \mu_t (I_i^h - I_i^e) \} , \quad (64)$$

$$G_4(\rho; z|z') = \mathfrak{S}_1 \left\{ \mu'_t \frac{(V_v^h - V_v^e)}{k_0 k_\rho} \right\} = \mathfrak{S}_1^0 \{ \mu'_t (V_v^h - V_v^e) \} , \quad (65)$$

$$G_5(\rho; z|z') = \mathfrak{S}_0 \left\{ \frac{(V_i^h + V_i^e)}{\eta_0 k_0^2} \right\} = \mathfrak{S}_0^1 \left\{ \frac{(V_i^h + V_i^e)}{\eta_0} \right\} , \quad (66)$$

$$G_6(\rho; z|z') = \mathfrak{S}_2 \left\{ \frac{(V_i^h - V_i^e)}{\eta_0 k_0^2} \right\} = \mathfrak{S}_2^1 \left\{ \frac{(V_i^h - V_i^e)}{\eta_0} \right\} , \quad (67)$$

$$G_7(\rho; z|z') = \mathfrak{S}_1 \left\{ \frac{k_\rho V_v^e}{k_0^3 \epsilon'_z} \right\} = \mathfrak{S}_1^2 \left\{ \frac{V_v^e}{\epsilon'_z} \right\} , \quad (68)$$

$$G_8(\rho; z|z') = \mathfrak{S}_1 \left\{ \frac{k_\rho I_i^e}{k_0^3 \epsilon_z} \right\} = \mathfrak{S}_1^2 \left\{ \frac{I_i^e}{\epsilon_z} \right\} , \quad (69)$$

$$G_9(\rho; z|z') = \mathfrak{S}_0 \left\{ \frac{k_\rho^2 \eta_0 I_v^e}{k_0^4 \epsilon'_z \epsilon_z} \right\} = \mathfrak{S}_0^1 \left\{ \frac{(k_\rho/k_0)^2 \eta_0 I_v^e}{\epsilon'_z \epsilon_z} \right\} , \quad (70)$$

$$G_{11}(\rho; z|z') = \mathfrak{S}_2 \left\{ \frac{(V_v^h - V_v^e)}{k_0^2} \right\} = \mathfrak{S}_2^1 \{ (V_v^h - V_v^e) \} , \quad (71)$$

$$G_{12}(\rho; z|z') = \mathfrak{S}_0 \left\{ \frac{(V_v^h + V_v^e)}{k_0^2} \right\} = \mathfrak{S}_0^1 \{ (V_v^h + V_v^e) \} , \quad (72)$$

$$G_{13}(\rho; z|z') = \mathfrak{S}_1 \left\{ \frac{k_\rho V_i^h}{k_0^3 \eta_0 \mu'_z} \right\} = \mathfrak{S}_1^2 \left\{ \frac{V_i^h}{\eta_0 \mu'_z} \right\} , \quad (73)$$

$$G_{14}(\rho; z|z') = \mathfrak{S}_1 \left\{ \frac{k_\rho \eta_0 I_v^e}{k_0^3 \epsilon_z} \right\} = \mathfrak{S}_1^2 \left\{ \frac{\eta_0 I_v^e}{\epsilon_z} \right\} . \quad (74)$$

Similarly, the kernels dual to (60)–(70) can be expressed as<sup>16</sup>

$$G'_0(\rho; z|z') = \mathfrak{S}_0 \left\{ \frac{\eta_0 (I_v^e - I_v^h)}{k_\rho^2} \right\} = \mathfrak{S}_0^1 \left\{ \frac{\eta_0 (I_v^e - I_v^h)}{(k_\rho/k_0)^2} \right\} , \quad (75)$$

$$G'_1(\rho; z|z') = \mathfrak{S}_0 \left\{ \frac{\eta_0 I_v^e}{k_0^2} \right\} = \mathfrak{S}_0^1 \{ \eta_0 I_v^e \} , \quad (76)$$

$$G'_2(\rho; z|z') = \mathfrak{S}_0 \left\{ \left( \frac{\epsilon_t}{\mu'_z} + \frac{\epsilon'_t}{\mu_z} \right) \frac{V_i^h}{\eta_0 k_0^2} + \epsilon_t \epsilon'_t \frac{(V_i^e - V_i^h)}{\eta_0 k_\rho^2} \right\} \quad (77)$$

$$= \mathfrak{S}_0^1 \left\{ \left( \frac{\epsilon_t}{\mu'_z} + \frac{\epsilon'_t}{\mu_z} \right) \frac{V_i^h}{\eta_0} + \epsilon_t \epsilon'_t \frac{(V_i^e - V_i^h)}{\eta_0 (k_\rho/k_0)^2} \right\} , \quad (78)$$

$$G'_3(\rho; z|z') = \mathfrak{S}_1 \left\{ \epsilon_t \frac{(V_v^e - V_v^h)}{k_0 k_\rho} \right\} = \mathfrak{S}_1^0 \{ \epsilon_t (V_v^e - V_v^h) \} , \quad (79)$$

---

<sup>16</sup>Note that we distinguish the dual kernels by primes.

$$G'_4(\rho; z|z') = \mathfrak{S}_1 \left\{ \epsilon'_t \frac{(I_i^e - I_i^h)}{k_0 k_\rho} \right\} = \mathfrak{S}_1^0 \{ \epsilon'_t (I_i^e - I_i^h) \} , \quad (80)$$

$$G'_5(\rho; z|z') = \mathfrak{S}_0 \left\{ \frac{\eta_0(I_v^e + I_v^h)}{k_0^2} \right\} = \mathfrak{S}_0^1 \{ \eta_0(I_v^e + I_v^h) \} , \quad (81)$$

$$G'_6(\rho; z|z') = \mathfrak{S}_2 \left\{ \frac{\eta_0(I_v^e - I_v^h)}{k_0^2} \right\} = \mathfrak{S}_2^1 \{ \eta_0(I_v^e - I_v^h) \} , \quad (82)$$

$$G'_7(\rho; z|z') = \mathfrak{S}_1 \left\{ \frac{k_\rho I_i^h}{k_0^3 \mu'_z} \right\} = \mathfrak{S}_1^2 \left\{ \frac{I_i^h}{\mu'_z} \right\} , \quad (83)$$

$$G'_8(\rho; z|z') = \mathfrak{S}_1 \left\{ \frac{k_\rho V_v^h}{k_0^3 \mu_z} \right\} = \mathfrak{S}_1^2 \left\{ \frac{V_v^h}{\mu_z} \right\} , \quad (84)$$

$$G'_9(\rho; z|z') = \mathfrak{S}_0 \left\{ \frac{k_\rho^2 V_i^h}{k_0^4 \eta_0 \mu'_z \mu_z} \right\} = \mathfrak{S}_0^1 \left\{ \frac{(k_\rho/k_0)^2 V_i^h}{\eta_0 \mu'_z \mu_z} \right\} . \quad (85)$$

It is understood that the primed and unprimed media parameters are to be evaluated in the source and field layers, respectively. The symbols  $\mathfrak{S}_n$  and  $\mathfrak{S}_n^m$  denote the integral operators

$$\mathfrak{S}_n \{ \cdot \} = \frac{1}{2\pi} \int_0^\infty \{ \cdot \} J_n(k_\rho \rho) k_\rho dk_\rho \quad (86)$$

and

$$\mathfrak{S}_n^m \{ \cdot \} = \frac{1}{2\pi} \int_0^\infty \{ \cdot \} J_n(k_\rho \rho) \left( \frac{k_\rho}{k_0} \right)^m d \left( \frac{k_\rho}{k_0} \right) , \quad (87)$$

respectively, where  $J_n$  is the Bessel function of order  $n$ . The integrals arising in (86)–(87) are referred to as Sommerfeld integrals and are discussed in more detail in the next section. The representation of the kernels in terms of  $\mathfrak{S}_n^m$  is convenient in the development of closed-form kernel representations. In Table 3 we list the combinations of  $n$  and  $m$  that occur in the basic kernels.

Table 3: Valid combinations of  $n$  and  $m$ .

$n$	0	1	2
$m$	1	0, 2	1

Note that 24 distinct basic and dual kernels are needed in general to determine the electric and magnetic fields due to electric and magnetic currents.

## 5 Direct computation of Sommerfeld integrals

As shown in the previous section, all basic and dual kernels can be expressed as Sommerfeld integrals (also known as Hankel transforms). The integrals that must be computed have the form

$$\mathfrak{S}_n \left\{ \tilde{G}(k_\rho|z, z') \right\} = \frac{1}{2\pi} \int_0^\infty \tilde{G}(k_\rho|z, z') J_n(k_\rho \rho) k_\rho dk_\rho \quad (88)$$

$$= \frac{1}{4\pi} \int_{\infty e^{-j\pi}}^\infty \tilde{G}(k_\rho|z, z') H_n^{(2)}(k_\rho \rho) k_\rho dk_\rho , \quad n = 0, 1, 2, \quad (89)$$

where the spectral-domain kernel  $\tilde{G}$  is an even (odd) function of  $k_\rho$  for even (odd)  $n$ ,<sup>17</sup>  $J_n$  is the Bessel function and  $H_n^{(2)}$  the Hankel function of the second kind, both of order  $n$ . The second integral form (89) can be derived from (88) by using the formulas  $J_n(z) = \frac{1}{2}[H_n^{(1)}(z) + H_n^{(2)}(z)]$  and  $H_n^{(1)}(ze^{j\pi}) = -e^{-jn\pi}H_n^{(2)}(z)$  [26].<sup>18</sup> The location of the integration path in (89) with respect to the pole and branch-point singularities is illustrated in Fig. 4. Note that only the positive-real

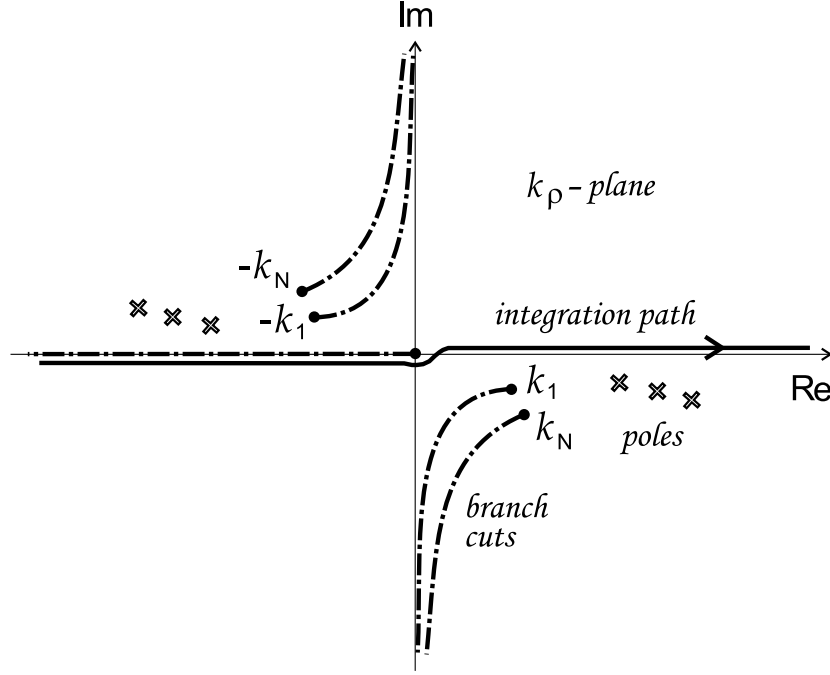


Figure 4: Sommerfeld integration path in the complex  $k_\rho$ -plane.

axis path is used in (88). The branch point at the origin is due to the Hankel function and it only occurs in the second integral form (89). The branch points at  $\pm k_1$  and  $\pm k_N$  are only present if the outermost layers are half-spaces, i.e., the multilayer is unshielded from below and above [27, p. 112]. The real-axis integration path in Fig. 4 can be deformed, as long as it does not cross any of the singular points.

Since the integration paths in (88)–(89) extend to infinity, it is important to understand the large- $k_\rho$  asymptotic form of the spectral domain kernels. Upon inspection of the relevant expressions, we find the dominant behavior as

$$\tilde{G}(k_\rho; z|z') \sim k_\rho^\mu e^{-k_\rho \zeta}, \quad k_\rho \rightarrow \infty, \quad (90)$$

where  $\zeta$  and  $\mu$  are coefficients that can be easily determined from the known asymptotic behavior of the TLGFs involved.<sup>19</sup> In isotropic media,  $\zeta$  is typically the vertical distance between the source and the field point,  $|z - z'|$ . For kernels  $G_3$ ,  $G_4$ , and  $G_{11}$ , the direct terms cancel when  $z$  and  $z'$  lie

<sup>17</sup>For simplicity, we omit the kernel index  $i$ .

<sup>18</sup>Strictly speaking, the integral in (89) should be taken in the principal value sense with respect to the origin. However, the small-argument behavior of the spectral domain kernels is such that the singularity of the Hankel function at the origin is always cancelled.

<sup>19</sup>The power coefficient  $\mu$  is unrelated to the same symbol used to denote permeability.

within the same isotropic layer  $n$ , in which case the coefficient  $\zeta$  is the smaller of  $(z + z') - 2z_n$  and  $2z_{n+1} - (z + z')$ . In uniaxial media, since

$$k_{zn}^\alpha \sim -jk_\rho/\lambda_n^\alpha \quad (91)$$

as  $k_\rho \rightarrow \infty$ ,  $\zeta$  is the vertical distance between the source and the field point, scaled by the anisotropy ratios of the layers. For example, if  $z$  and  $z'$  are within the same layer  $n$ , then  $\zeta = |z - z'|/\lambda_n^\alpha$ . The value of  $\mu$  readily follows from Table 2. Taking into account the large-argument form of the Bessel function, we find that the asymptotic behavior of the entire integrand in (88) is given by (90) with  $\mu \rightarrow \mu - 0.5$ . Clearly, the worst case arises for  $\zeta = 0$ , when the exponential decay factor is absent and the integrand is oscillatory, and possibly divergent.

To compute the Sommerfeld integrals, we employ the *integration-then-summation* procedure [1], applied to the first integral form (88). As illustrated in Fig. 5, the integration path is deformed into the first quadrant of the  $k_\rho$ -plane to avoid the branch-point and pole singularities that may lie on or close to the real axis [1, 28–30]. The exact shape of the initial path segment is not critical,

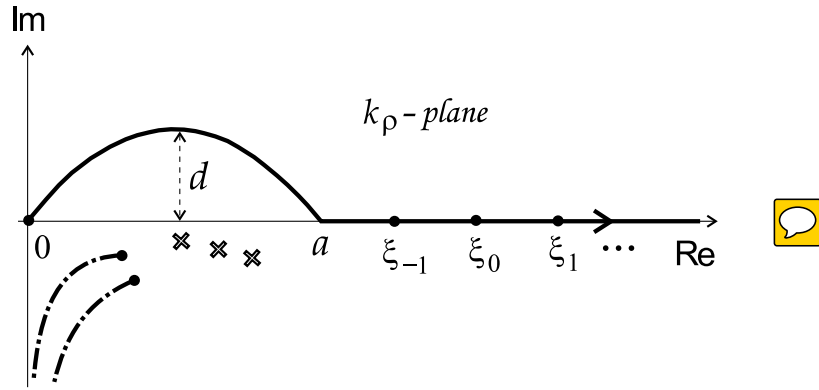


Figure 5: Deformed integration path with break points.

and we use a half-sine shape, with  $a/k_0 = n_{\max} + 1$ , where  $n_{\max}$  is the maximum real part of the effective refractive indices  $n_{\text{eff}}^\alpha$  of the multilayer, given by (24). The maximum sine height  $d$  is limited by the exponential growth of the Bessel function when  $k_\rho$  departs from the real axis. Hence, we set<sup>20</sup>

$$d/k_0 = \begin{cases} \min\left(1, \frac{1}{k_0\rho}\right), & \text{if } \rho > \zeta', \\ 1, & \text{otherwise,} \end{cases} \quad (92)$$

where  $\zeta' = \text{Re}\{\zeta\}$ . From the point  $a$  on, the integration follows the real axis, using the *break points*  $\xi_i$ ,  $i = -1, 0, 1, \dots$ , which are selected, as follows. If  $\rho > \zeta'$ , we use consecutive, approximate Bessel function extrema, computed as average values of the adjacent Bessel function zeros,<sup>21</sup> with  $\xi_{-1}$  set to the first extremum exceeding  $a$ ; otherwise, we use uniformly spaced break points separated by a fixed-length interval  $\Delta\xi = \pi/\zeta'$ , with  $\xi_{-1} = a + \min(a, \Delta\xi)$ .<sup>22</sup>

<sup>20</sup>This is admittedly a somewhat arbitrary choice and some other values may work as well.

<sup>21</sup>Tabulated values are used for the first ten Bessel function zeros, and asymptotic values otherwise [26].

<sup>22</sup>Again, these are somewhat arbitrary choices, which have been found to work well.

We may now express a typical Sommerfeld integral as

$$\mathfrak{S}_n \left\{ \tilde{G}(k_\rho | z, z') \right\} = I_a + I_b + I_\infty, \quad (93)$$

where the right-hand terms are defined as follows.  $I_a$  is the integral along the deformed path segment, given as

$$I_a = \frac{1}{2\pi} \int_0^a \tilde{G}(k_\rho; z|z') J_n(k_\rho \rho) k_\rho \left( \frac{dk_\rho}{dt} \right) dt, \quad (94)$$

where

$$k_\rho = t + jd \sin(\pi t/a) \quad (95)$$

and  $t$  is a real parameter.  $I_b$  is the real-axis integral from  $a$  to the first break point, given as

$$I_b = \frac{1}{2\pi} \int_a^{\xi-1} \tilde{G}(k_\rho; z|z') J_n(k_\rho \rho) k_\rho dk_\rho. \quad (96)$$

$I_\infty$  is the real-axis *tail integral*, given as

$$I_\infty = \frac{1}{2\pi} \int_{\xi-1}^\infty \tilde{G}(k_\rho; z|z') J_n(k_\rho \rho) k_\rho dk_\rho = \sum_{i=0}^\infty u_i, \quad (97)$$

where

$$u_i = \frac{1}{2\pi} \int_{\xi_{i-1}}^{\xi_i} \tilde{G}(k_\rho; z|z') J_n(k_\rho \rho) k_\rho dk_\rho. \quad (98)$$

The integrals  $I_a$  and  $I_b$  are computed by an adaptive quadrature based on the Patterson rule [31], and the *partial integrals*  $u_i$  are computed by a Gauss-Legendre quadrature<sup>23</sup> of order 16.

As indicated in (97), the tail integral is evaluated as an infinite sum of the partial integrals (98). It can be shown [1] that for  $\rho > 0$ , the series of partial integrals is asymptotically alternating, with logarithmic convergence for  $\zeta = 0$  and linear convergence for  $\zeta \neq 0$ . For  $\rho = 0$  and  $\zeta \neq 0$ , the convergence is monotone linear. We compute this series as the limit of the sequence of *partial sums*

$$s_n = \sum_{i=0}^n u_i, \quad (99)$$

as  $n \rightarrow \infty$ . To accelerate the convergence, we use the weighted-averages extrapolation method, given as [1, 2, 32]

$$s_n^{(k)} = \frac{s_n^{(k-1)} + \eta_n^{(k-1)} s_{n+1}^{(k-1)}}{1 + \eta_n^{(k-1)}}, \quad n \geq 0, \quad k \geq 1, \quad (100)$$

with the *weights*

$$\eta_n^{(k)} = \pm \left( \frac{\xi_{n+1}}{\xi_n} \right)^{2k-\alpha} e^{(\xi_{n+1}-\xi_n)\zeta}, \quad (101)$$

---

<sup>23</sup>Paradoxically, using the adaptive Patterson quadrature for the partial integrals can be unreliable in the case of exponential decay, because the integrands can sometimes become negligibly small and the adaptive rule can fail trying to integrate what is essentially numerical noise.



where  $\alpha = \mu + 1/2$ .<sup>24</sup> Here, the upper and lower signs apply to the alternating ( $\rho > \zeta'$ ) and monotone ( $\rho \leq \zeta'$ ) convergence cases, respectively. The recursion (100) represents a triangular scheme, which after the third step has the form

$$\begin{array}{ccccccc} s_0^{(0)} & s_0^{(1)} & s_0^{(2)} & s_0^{(3)} & \cdot & & \\ s_1^{(0)} & s_1^{(1)} & s_1^{(2)} & \cdot & & & \\ s_2^{(0)} & s_2^{(1)} & \cdot & & & & \\ s_3^{(0)} & \cdot & & & & & \\ \cdot & & & & & & \end{array} \quad (102)$$

where in the first column  $s_n^{(0)} = s_n$ . At step  $i$ , the computations start at the lowest table element and proceed upwards along the counterdiagonal  $i = n + k$ . Note that only a one-dimensional array, storing the counterdiagonal elements, is needed to implement this scheme, as the newly-generated entries can overwrite the no longer needed elements from the previous iteration. Hence, given the partial sums  $s_0, s_1, \dots, s_i$ , the weighted-averages algorithm produces  $s_0^{(i)}$  as the best approximation of the tail integral  $I_\infty$ . The recursion is applied with an increasing  $i$  until the outcomes of two consecutive iterations do not differ by more than a prescribed small error threshold.

The rigorous integration procedure outlined here has been implemented to provide benchmark results for the complex image method described in the following sections. Hence, with a few exceptions, the spectral functions are integrated directly, with no pre-processing. For kernels  $G_7$ ,  $G_8$ , and their dual kernels, convergence problems were encountered for  $k_0\rho < 10^{-2}$  when  $z'$  and  $z$  both lie on the same interface between dissimilar layers. These were remedied by subtracting from the spectral domain kernels their leading quasi-static terms, which integrate to zero.

The approach presented here is only recommended for small to moderate values of  $k_0\rho$ , up to about  $10^2$ . This limitation is due to the rapid integrand oscillations on the initial path segment in Fig. 5 when  $k_\rho\rho$  becomes large in magnitude, and the fact that in this case the path passes very near the real-axis singularities of the spectral domain kernels, as a consequence of (92). The range of applicability of this method can be extended by choosing different integration paths. For example, using the second integral form (89) as the point of departure, one can wrap the integration contour around the branch cuts, where the integrands are rapidly convergent for large  $\rho$  [33, 34]. Furthermore, one can deform the integration path into a steepest descent path, where the integrand converges exponentially. These methods, however, require the tracking of any poles (including improper ones) that may be captured by the path deformation [35–37].

## 6 Application of the discrete complex image method

The high cost of the direct integration of the Sommerfeld integrals has prompted us to also implement the so-called discrete complex image method (DCIM) [3–5, 7, 9, 34, 38–42]. As mentioned at the end of Sec. 4, in the context of DCIM we use the representation

$$G(\rho; z|z') = \mathfrak{S}_n^m \left\{ \tilde{G}(k_\rho; z|z') \right\}, \quad (103)$$

<sup>24</sup>In the above,  $n$  is unrelated to the same symbol used for the order of the Bessel function or layer index. Also,  $\eta$  must not be confused with the same symbol used for intrinsic impedance, and  $\alpha$  is unrelated the same symbol used to distinguish TM and TE waves.

where  $\tilde{G}$  is now referred to as the spectral domain kernel. The key step in this approach is the exponential fit of  $\tilde{G}$  along a specified path in the complex spectral plane. The exponential terms, which may be interpreted as contributions due to complex images of the point source, can be inverted in closed form, resulting in an efficient procedure. The robustness of this method is usually improved if the quasi-static form of the kernel, corresponding to  $k_\rho \rightarrow \infty$ , is first extracted and handled analytically. Similarly, it is also desirable to extract the guided wave terms and branch point terms from the spectral kernel before the exponential fit is performed. Hence, the exponential fit is usually applied to the *remainder kernel* after all important physical constituents have been subtracted out.

## 6.1 Extraction of quasi-static terms

For each spectral-domain kernel  $\tilde{G}$ , we wish to find its quasi-static form  $\tilde{G}^q$ , which possesses the property that  $\tilde{G} \sim \tilde{G}^q$  as  $k_\rho \rightarrow \infty$ , and which can be transformed to the space domain in closed form. Since the spectral-domain kernels in (60)–(85) comprise the TLGFs,  $\tilde{G}^q$  is easily found, once the quasi-static forms of the TLGFs are determined. As alluded to in Sec. 3, the TLGFs could also be computed by summing the infinite number of rays that originate at the source and undergo multiple reflections and transmissions at the interfaces between layers before reaching the observation point. Here, we are only interested in extracting a small number of *dominant* rays,<sup>25</sup> in the quasi-static regime that corresponds to  $k_\rho \rightarrow \infty$ . In this regime, the characteristic impedances of layer  $n$  behave as

$$\frac{Z_n^e}{\eta_0} \sim \frac{k_\rho}{jk_0\kappa_n^e}, \quad \frac{Z_n^h}{\eta_0} \sim \frac{jk_0\kappa_n^h}{k_\rho}, \quad (104)$$

where we have introduced the notation

$$\kappa_n^e = \sqrt{\epsilon_{tn}\epsilon_{zn}}, \quad \kappa_n^h = \sqrt{\mu_{tn}\mu_{zn}}. \quad (105)$$

Using the above, it is found that the Fresnel reflection coefficients at an interface between layers  $j$  and  $i$  behave as

$$\Gamma_{i,j}^e \sim -\frac{\kappa_i^e - \kappa_j^e}{\kappa_i^e + \kappa_j^e}, \quad \Gamma_{i,j}^h \sim \frac{\kappa_i^h - \kappa_j^h}{\kappa_i^h + \kappa_j^h}, \quad (106)$$

with the corresponding transmission coefficients given as

$$T_{i,j}^\alpha = 1 + \Gamma_{i,j}^\alpha. \quad (107)$$

To make a closed-form inversion of the extracted quasi-static rays possible, we define an “equivalent medium” of a multilayer as a homogeneous, isotropic medium characterized by the wavenumber  $k_q = k_0 n_q$ , where  $n_q$  is set to the effective refractive index  $n_{\text{eff},n}^\alpha$  with a minimum real part.<sup>26</sup> The corresponding propagation constant is thus

$$k_{zq} = \sqrt{k_q^2 - k_\rho^2}, \quad (108)$$

<sup>25</sup>The dominant rays are those with the shortest paths of travel, and thus having the slowest decay rates for large  $k_\rho$ .

<sup>26</sup>Perhaps a more obvious choice would be to set  $n_q$  to the transverse refractive index of the field-point layer. However, numerical experiments (not reported here) have shown that the present choice results in a better performance of the DCIM.

with  $jk_{zq} \sim k_\rho$  as  $k_\rho \rightarrow \infty$ . Note that a wave traveling a distance  $d$  in a TL section corresponding to layer  $n$  gives rise to the exponential factor

$$e^{-jk_{zn}^\alpha d} \sim e^{-jk_{zq}d/\lambda_n^\alpha} \sim e^{-k_\rho d/\lambda_n^\alpha}. \quad (109)$$

Hence, in the quasi-static problem the distances along  $z$  are scaled by the inverse anisotropy ratios, as previously indicated in connection with (91). Note the asymptotic equivalence

$$k_{zn}^\alpha \sim k_{zq}/\lambda_n^\alpha. \quad (110)$$

We describe the quasi-static term extraction with reference to the TLGFs (36)–(37) and illustrate the ray tracing procedure in Fig. 6.<sup>27</sup> For each interface  $i$ , we pre-compute the upward-looking TM and TE static Fresnel reflection coefficients  $R_i^\alpha$ , based on (106).<sup>28</sup> We assume that the source is in layer  $n$  of the multilayer. Since the factors  $Z_n/2$ ,  $Y_n/2$ , or  $1/2$  are common to all rays, they are omitted in the ray tracing, but are restored (in their quasi-static form) at a later stage.

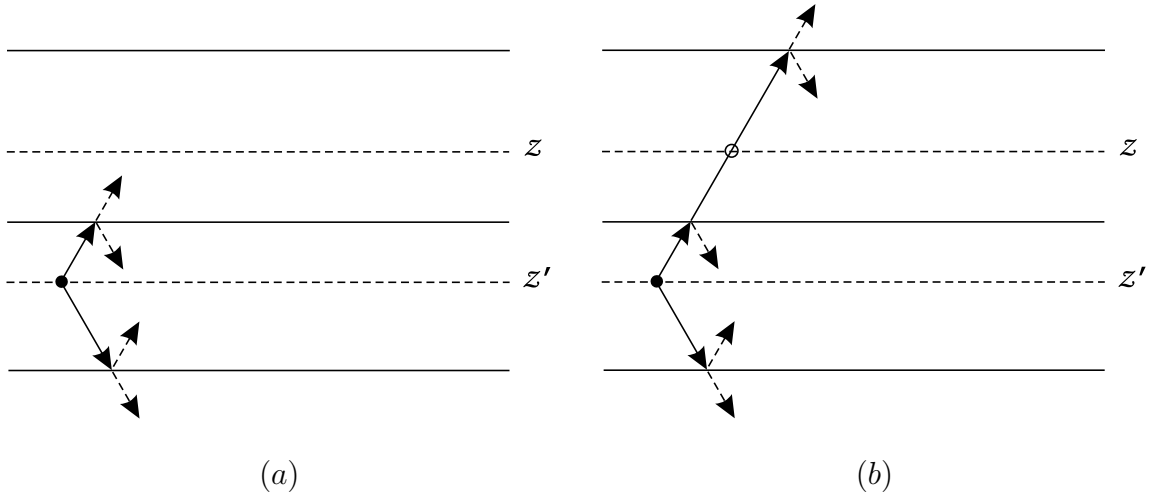


Figure 6: Illustration of the ray tracing for quasi-static term extraction. (a) The up-going incident ray originating at the source gives rise to an up-going transmitted ray and a down-going reflected ray at the upper interface. Similarly, the down-going incident ray generates an up-going reflected ray and a down-going transmitted ray at the lower interface. (b) The ray with the shortest travel path—assumed to be the up-going ray at the upper interface of the source layer—is propagated to the next interface, where it creates an up-going transmitted ray and a down-going reflected ray. A quasi-static term is extracted (indicated by a circle), since the up-propagated ray crosses the field-point level.

The ray tracing begins by launching from the source in layer  $n$  two rays, one going up, with amplitude  $+1$ , and one going down, with amplitude  $+1$  for  $V_i$  and  $I_v$ , and  $-1$  for  $I_i$  and  $V_v$ .<sup>29</sup>

<sup>27</sup>A similar procedure described in [10] assumes that the source and the field point lie on interfaces of the multilayer. Hence, if in the original layered medium the source or the field point is not situated at an interface, the layer containing it must be split into two layers with the same material properties, by introducing a virtual interface. This approach becomes cumbersome when  $z$  or  $z'$  are varying.

<sup>28</sup>The down-looking reflection coefficients are simply the negatives of  $R_i^\alpha$ . It is worth noting that for nonmagnetic media  $R_i^h = 0$  at all dielectric interfaces.

<sup>29</sup>For simplicity, where there is no danger of confusion, we omit the superscript  $\alpha$ .

If the observation point is in the source layer, the direct ray is first *extracted*,<sup>30</sup> with amplitude  $+1$  for  $V_i$  and  $I_v$ , and  $+1$  or  $-1$  for  $I_i$  and  $V_v$ , depending on whether  $z > z'$  or  $z < z'$ , respectively.<sup>31</sup> The quasi-static path traveled by this ray is  $|z - z'|/\lambda_n$ . The up-going ray hits interface  $n + 1$ , where it gives rise to a reflected ray with amplitude  $R_{n+1}$  and a transmitted ray with amplitude  $T_{n+1} = 1 + R_{n+1}$ .<sup>32</sup> The quasi-static path traveled by this ray is  $(z_{n+1} - z')/\lambda_n$ . Similarly, the down-going ray hits interface  $n$ , where it creates reflected and transmitted rays with amplitudes  $-R_n$  and  $T_n = 1 - R_n$ , respectively, possibly multiplied by  $-1$  (in the case of  $I_i$  and  $V_v$ ). The quasi-static path traveled by this ray is  $(z' - z_n)/\lambda_n$ .

The initial four rays are propagated up and down and hit the adjacent interfaces, where they are partially transmitted and partially reflected, each giving rise to another pair of up- and down-going rays, whose amplitudes are modified by the appropriate static Fresnel reflection or transmission coefficients. The phases of these rays, which correspond to the quasi-static path lengths traveled, are accumulated and stored. This procedure is then repeated for each of the so-created rays. Each time a ray crosses the field-point level, it is extracted.

In theory, assuming that there are at least two non-trivial interfaces present, this procedure would continue forever, since the number of rays is infinite. To remedy this, we prioritize the rays and terminate the procedure after extracting the desired number of dominant rays, with the shortest travel paths between the source and the field point. To this end, each ray is assigned a *key*, which is the real part of its accumulated phase. At each step of the ray tracing procedure, the ray with the lowest key is processed first, since the lowest key corresponds to the shortest *electrical path* traveled. To keep track of the rays with the highest priorities, we use the *priority queue* algorithm [43], as first proposed in [10]. The priority queue algorithm exploits the so called min-heap data structure, where each parent element has two children elements, arranged such that the keys of the children never exceed the key of their parent. In our case, each heap element represents a ray with all its attributes, such as the key, amplitude, phase, interface index, and the direction of travel (up or down). The priority queue algorithm supports two operations, `PUSH` and `POP`, where `PUSH` inserts an element into the heap and `POP` returns and removes the element with the smallest key. Following each of these operations the heap is updated to maintain the min-heap property.

Hence, our quasi-static part extraction algorithm may now be summarized as follows. First, the initial four rays generated by the source, as illustrated in Fig. 6(a), are `PUSHed` on the heap, and the direct term is extracted if the observation point lies in the source layer. Then, the highest-priority ray is `POPped` off the heap, propagated to the next interface, and the resulting reflected and transmitted rays are `PUSHed` back onto the heap. If a ray crosses the field-point level, it is extracted, as illustrated in Fig. 6(b). Should the extracted ray have the same phase as one of the previously extracted rays, it is merged with that ray. This extraction process continues until the desired number of quasi-static terms is reached, or the heap is exhausted.

Even though the rays are processed in the order of their priority, there is no guarantee that the dominant rays are extracted strictly in the order of increasing path lengths. This is because the highest priority ray entering the field-point layer may have a longer path to the field point than the next in priority ray entering this layer from the opposite side. Furthermore, the last few extracted rays may be incomplete, since there is a possibility that a later ray would be merged with an already

<sup>30</sup>Here, by “extracting” a ray we mean computing and recording its amplitude and path length traveled.

<sup>31</sup>Note that if  $z = z'$ , additional information is required to decide whether  $z = z' + 0$  or  $z = z' - 0$ .

<sup>32</sup>Here, the voltage or current reflection coefficients are implied, depending on the type of the TLGFs involved. The current reflection coefficient is simply the negative of the corresponding voltage reflection coefficient.

extracted ray and modify its amplitude. Hence, in order to be reasonably sure that a sequence of complete dominant rays is obtained, we extract several more rays than the desired number, sort them in the ascending order of their keys, and discard the superfluous ones.

Taking  $V_i^e$  as an example, the above algorithm will produce the quasi-static representation

$$V_i^e(z|z') \sim \frac{\eta_0 k_\rho}{2j\kappa_n^e k_0} \sum_{i=1}^{N_e} a_{qi}^e e^{-jk_{zq} b_{qi}^e}, \quad (111)$$

where the subscript  $n$  is the index of the source layer,  $N_e$  is the number of dominant quasi-static rays extracted,  $a_{qi}^e$  are the ray amplitudes, and  $b_{qi}^e$  are the corresponding path lengths traveled (or phases, for short).<sup>33</sup> The factor in front of the sum is the restored  $Z_n^e/2$  starting ray amplitude, with  $Z_n^e$  replaced by the quasi-static form given in (104).

Since many of the spectral-domain kernels in (60)–(85) comprise two TLGFs, two sets of quasi-static terms are in general involved. In the case of  $\tilde{G}_0$ , we have

$$\tilde{G}_0 \sim \frac{(V_i^h - V_i^e)}{\eta_0(k_\rho/k_0)^2} \sim \tilde{G}_0^q, \quad (112)$$

which leads to

$$\tilde{G}_0^q = \frac{j}{2\kappa_n^e} \frac{1}{jk_{zq}} \sum_{i=1}^{N_e} a_{qi}^e e^{-jk_{zq} b_{qi}^e}, \quad (113)$$

where we used (111) and the asymptotic equivalence of  $k_\rho$  and  $jk_{zq}$ . In deriving this expression we neglected  $V_i^h$  in favor of the asymptotically dominant  $V_i^e$  (see Table 2), which was necessary, because the quasi-static form of  $V_i^h/k_\rho^2$  does not have a closed-form inverse. In the above and henceforth, we assume that  $k_{zq}$  is normalized to  $k_0$ .

In the case of  $\tilde{G}_1$ , we have

$$\tilde{G}_1 = \frac{V_i^h}{\eta_0} \sim \tilde{G}_1^q, \quad (114)$$

which leads to

$$\tilde{G}_1^q = \frac{j\kappa_n^h}{2} \frac{1}{jk_{zq}} \sum_{i=1}^{N_h} a_{qi}^h e^{-jk_{zq} b_{qi}^h}, \quad (115)$$

where the sum represents the quasi-static rays extracted from  $V_i^h$ . In the factor preceding the sum, we used (110).

In the case of  $\tilde{G}_2$ , we have

$$\tilde{G}_2 \sim \left( \frac{\mu_{tm}}{\epsilon_{zn}} + \frac{\mu_{tn}}{\epsilon_{zm}} \right) \eta_0 I_v^e + \mu_{tm} \mu_{tn} \frac{\eta_0 (I_v^h - I_v^e)}{(k_\rho/k_0)^2} \sim \tilde{G}_2^q, \quad (116)$$

---

<sup>33</sup>Here and in what follows, the superscripts  $e$  or  $h$  are used to distinguish the quasi-static coefficients (ray amplitudes and phases) associated with the TM and TE TLGFs, respectively. For simplicity, the same symbols will be used for the quasi-static coefficients associated with the voltage- and current-type TLGFs. It will be evident from the context which TLGF type is implied.

where the subscript  $m$  is the index of the field-point layer. Upon applying the quasi-static ray extraction algorithm to the two TLGFs, we obtain

$$\begin{aligned}\tilde{G}_2^q = & \left( \frac{\mu_{tm}}{\epsilon_{zn}} + \frac{\mu_{tn}}{\epsilon_{zm}} \right) \frac{j\kappa_n^e}{2} \frac{1}{jk_{zq}} \sum_{i=1}^{N_e} a_{qi}^e e^{-jk_{zq}b_{qi}^e} \\ & - \frac{j\mu_{tm}\mu_{tn}}{2\kappa_n^h} \frac{1}{jk_{zq}} \sum_{i=1}^{N_h} a_{qi}^h e^{-jk_{zq}b_{qi}^h},\end{aligned}\quad (117)$$

where the first and the second sums represent the quasi-static rays extracted from  $I_v^e$  and  $I_v^h$ , respectively. In deriving this expression, in the second term of  $\tilde{G}_2$  we neglected  $I_v^e$  in favor of the asymptotically dominant  $I_v^h$  (see Table 2). This was necessary, because the quasi-static form of  $I_v^e/k_\rho^2$  does not have a closed-form inverse.

In the case of  $\tilde{G}_3$ , we have

$$\tilde{G}_3 = \mu_{tm}(I_i^h - I_i^e) \sim \tilde{G}_3^q, \quad (118)$$

which leads to

$$\tilde{G}_3^q = \frac{\mu_{tm}}{2} \left( \sum_{i=1}^{N_h} a_{qi}^h e^{-jk_{zq}b_{qi}^h} - \sum_{i=1}^{N_e} a_{qi}^e e^{-jk_{zq}b_{qi}^e} \right), \quad (119)$$

where the first and second sums represent the quasi-static rays extracted from  $I_i^h$  and  $I_i^e$ , respectively.

In the case of  $\tilde{G}_4$ , we have

$$\tilde{G}_4 = \mu_{tn}(V_v^h - V_v^e) \sim \tilde{G}_4^q, \quad (120)$$

which leads to

$$\tilde{G}_4^q = \frac{\mu_{tn}}{2} \left( \sum_{i=1}^{N_h} a_{qi}^h e^{-jk_{zq}b_{qi}^h} - \sum_{i=1}^{N_e} a_{qi}^e e^{-jk_{zq}b_{qi}^e} \right), \quad (121)$$

where the first and second sums represent the quasi-static rays extracted from  $V_v^h$  and  $V_v^e$ , respectively.

In the case of  $\tilde{G}_5$ , we have

$$\tilde{G}_5 = \frac{(V_i^h + V_i^e)}{\eta_0} \sim \tilde{G}_5^q, \quad (122)$$

which leads to

$$\tilde{G}_5^q = \frac{1}{2j\kappa_n^e} jk_{zq} \sum_{i=1}^{N_e} a_{qi}^e e^{-jk_{zq}b_{qi}^e} + \frac{j\kappa_n^h}{2} \frac{1}{jk_{zq}} \sum_{i=1}^{N_h} a_{qi}^h e^{-jk_{zq}b_{qi}^h}, \quad (123)$$

where the first and second sums represent the quasi-static rays extracted from  $V_i^h$  and  $V_i^e$ , respectively. Note that (123) comprises two quasi-static forms, with the first asymptotically dominant.

Although the second form can be omitted, we retain it in order to make  $\tilde{G}_5^q$  exact in the case of isotropic, homogeneous multilayers.<sup>34</sup> Kernels other than  $G_5$  do not require this special treatment.

In the case of  $\tilde{G}_6$ , we have

$$\tilde{G}_6 = \frac{(V_i^h - V_i^e)}{\eta_0} \sim (k_\rho/k_0)^2 \tilde{G}_6^q, \quad (124)$$

which leads to

$$\tilde{G}_6^q = \frac{j}{2\kappa_n^e} \frac{1}{jk_{zq}} \sum_{i=1}^{N_e} a_{qi}^e e^{-jk_{zq}b_{qi}^e}, \quad (125)$$

where the sum represents the quasi-static rays extracted from  $V_i^e$ . In deriving this expression, which is identical to (113), we again neglected  $V_i^h$  in favor of the dominant  $V_i^e$ .

In the case of  $\tilde{G}_7$ , we have

$$\tilde{G}_7 = \frac{V_v^e}{\epsilon_{zn}} \sim \tilde{G}_7^q, \quad (126)$$

which leads to

$$\tilde{G}_7^q = \frac{1}{2\epsilon_{zn}} \sum_{i=1}^{N_e} a_{qi}^e e^{-jk_{zq}b_{qi}^e}, \quad (127)$$

where the sum represents the quasi-static rays extracted from  $V_v^e$ .

In the case of  $\tilde{G}_8$ , we have

$$\tilde{G}_8 = \frac{I_i^e}{\epsilon_{zm}} \sim \tilde{G}_8^q, \quad (128)$$

which leads to

$$\tilde{G}_8^q = \frac{1}{2\epsilon_{zm}} \sum_{i=1}^{N_e} a_{qi}^e e^{-jk_{zq}b_{qi}^e}, \quad (129)$$

where the sum represents the quasi-static rays extracted from  $I_i^e$ .

In the case of  $\tilde{G}_9$ , we have

$$\tilde{G}_9 = \frac{(k_\rho/k_0)^2 \eta_0 I_v^e}{\epsilon_{zn} \epsilon_{zm}} \sim (k_\rho/k_0)^2 \tilde{G}_9^q, \quad (130)$$

which leads to

$$\tilde{G}_9^q = \frac{j\kappa_n^e}{2\epsilon_{zn} \epsilon_{zm}} \frac{1}{jk_{zq}} \sum_{i=1}^{N_e} a_{qi}^e e^{-jk_{zq}b_{qi}^e}, \quad (131)$$

where the sum represents the quasi-static rays extracted from  $I_v^e$ .

In the case of  $\tilde{G}_{11}$ , we have

$$\tilde{G}_{11} = (V_v^h - V_v^e) \sim \tilde{G}_{11}^q, \quad (132)$$

---

<sup>34</sup>This is a desirable property, because it makes the subsequent exponential fit unnecessary. Here, we are referring to a situation where all layers, including half-spaces, are made of the same isotropic material. This multilayer may be unshielded or backed on one side by a PEC or PMC groundplane. In this case, the number of quasi-static terms is reduced to one for the unshielded geometry, since only the direct ray is present, and to two for the grounded structure, since the ray reflected from the groundplane must also be included. Note that kernels  $G_3$ ,  $G_4$ , and  $G_{11}$  are identically zero in this case, since  $I_i^e = I_i^h$  and  $V_v^e = V_v^h$ .

which leads to

$$\tilde{G}_{11}^q = \frac{1}{2} \left( \sum_{i=1}^{N_h} a_{qi}^h e^{-jk_{zq}b_{qi}^h} - \sum_{i=1}^{N_e} a_{qi}^e e^{-jk_{zq}b_{qi}^e} \right), \quad (133)$$

where the first and second sums represent the quasi-static rays extracted from  $V_v^h$  and  $V_v^e$ , respectively.

In the case of  $\tilde{G}_{12}$ , we have

$$\tilde{G}_{12} = (V_v^h + V_v^e) \sim \tilde{G}_{12}^q, \quad (134)$$

which leads to

$$\tilde{G}_{12}^q = \frac{1}{2} \left( \sum_{i=1}^{N_h} a_{qi}^h e^{-jk_{zq}b_{qi}^h} + \sum_{i=1}^{N_e} a_{qi}^e e^{-jk_{zq}b_{qi}^e} \right), \quad (135)$$

where the first and second sums represent the quasi-static rays extracted from  $V_v^h$  and  $V_v^e$ , respectively.

In the case of  $\tilde{G}_{13}$ , we have

$$\tilde{G}_{13} = \frac{V_i^h}{\eta_0 \mu_{zn}} \sim \tilde{G}_{13}^q, \quad (136)$$

which leads to

$$\tilde{G}_{13}^q = \frac{j\kappa_n^h}{2\mu_{zn}} \frac{1}{jk_{zq}} \sum_{i=1}^{N_h} a_{qi}^h e^{-jk_{zq}b_{qi}^h}, \quad (137)$$

where the sum represents the quasi-static rays extracted from  $V_i^h$ .

In the case of  $\tilde{G}_{14}$ , we have

$$\tilde{G}_{14} = \frac{\eta_0 I_v^e}{\epsilon_{zm}} \sim \tilde{G}_{14}^q, \quad (138)$$

which leads to

$$\tilde{G}_{14}^q = \frac{j\kappa_n^e}{2\epsilon_{zm}} \frac{1}{jk_{zq}} \sum_{i=1}^{N_e} a_{qi}^e e^{-jk_{zq}b_{qi}^e}, \quad (139)$$

where the sum represents the quasi-static rays extracted from  $I_v^e$ .

In what follows, we assume that all  $k_\rho$ -independent factors have been absorbed into the coefficients  $a_{qi}^\alpha$ . For kernels comprising two TLGFs, the two quasi-static forms are merged whenever possible, to minimize the total number of quasi-static terms. In the case of  $\tilde{G}_3$ ,  $\tilde{G}_4$ , and  $\tilde{G}_{11}$ , the direct rays associated with the two TLGFs cancel, if the source and the field point lie in the same isotropic layer. However, if these points lie on the same interface between dissimilar media, the corresponding space-domain kernels are still singular.

In summary, after the post-processing described above, the quasi-static parts will have one of the three forms given below.

1. For  $G_0$ ,  $G_1$ ,  $G_2$ ,  $G_6$ ,  $G_9$ ,  $G_{13}$ , and  $G_{14}$ ,

$$\tilde{G}^q = \frac{1}{jk_{zq}} \sum_{i=1}^{N_q} a_{qi} e^{-jk_{zq}b_{qi}}. \quad (140)$$



2. For  $G_5$ ,

$$\tilde{G}^q = jk_{zq} \sum_{i=1}^{N_{q1}} a_{q1i} e^{-jk_{zq}b_{q1i}} + \frac{1}{jk_{zq}} \sum_{i=1}^{N_{q2}} a_{q2i} e^{-jk_{zq}b_{q2i}}. \quad (141)$$

3. For  $G_3, G_4, G_7, G_8, G_{11}$ , and  $G_{12}$ ,

$$\tilde{G}^q = \sum_{i=1}^{N_q} a_{qi} e^{-jk_{zq}b_{qi}}. \quad (142)$$

Note that the quasi-static representation of  $G_5$  comprises two quasi-static forms, with the first asymptotically dominant. As already mentioned, the second form could be omitted, but we retain it in order to make  $\tilde{G}^q$  exact in the case of isotropic, homogeneous multilayers.

The space-domain counterparts of (140)–(142) can be obtained by using the integral identities listed in Appendix A. The treatment of the dual kernels  $\tilde{G}'_0$  through  $\tilde{G}'_9$  is completely analogous to that of the corresponding basic kernels and is not presented here in the interest of brevity.

## 6.2 Extraction of guided-wave terms

The spectral domain kernels in general possess branch-point and pole singularities, as indicated in Fig. 4. Given the geometry of the multilayer and the media parameters, the location of all poles can be automatically computed, as described in detail elsewhere [44]. We use a modified Delves-Lyness method [23, 24] employing a polygonal contour integration technique [45] and a  $k_\rho$ –plane mapping [46–49] to remove branch points. Note that there are in general two sets of poles, associated with the TM and TE waves.

The pole residues of the spectral domain kernels in (60)–(85) can readily be computed from the residues of the TLGFs of the multilayer.<sup>35</sup> Hence, let  $\text{TLGF}_k^\alpha$  denote one of the four TLGFs listed in Table 1, where the subscript  $k$  ( $= 1, 2, 3, 4$ ) denotes the TLGF number and the superscript  $\alpha$  ( $= e, h$ ) the wave type. Also, let  $k_{\rho i}^\alpha$  be the  $i$ th pole of type  $\alpha$ . Then, the corresponding TLGF residue can be found as

$$R_{ki}^\alpha = \frac{a}{2\pi} \int_0^{2\pi} \text{TLGF}_k^\alpha(k_\rho; z|z') \Big|_{k_\rho=k_{\rho i}^\alpha + a e^{j\varphi}} e^{j\varphi} d\varphi, \quad (143)$$

where  $a$  is the radius of a circular path centered at the pole, selected not to exceed half the distance from  $k_{\rho i}^\alpha$  to the nearest  $k_\rho$ –plane singularity. The integral is computed by an adaptive trapezoidal quadrature.

The relationship between the kernel residues,  $R_{ki}^\alpha$ , and the TLGF residues,  $R_{ki}^\alpha$ , is given in Table 4. As before, the subscripts  $n$  and  $m$  are used to distinguish media parameters of the source and field-point layers, respectively. Also, it is assumed that in the computation of the TLGF residues the normalizations  $V_i/\eta_0 \rightarrow V_i$  and  $\eta_0 I_v \rightarrow I_v$  are used, and that the poles  $k_{\rho i}^\alpha$  are normalized to  $k_0$ . The residues of the kernels  $G'_0$  through  $G'_9$ , which are given by expressions dual to those listed for the kernels  $G_0$  through  $G_9$ , are omitted for brevity.

Let us now suppose that a spectral domain kernel  $\tilde{G}$  has  $N_p$  poles  $k_{\rho i}$  on the positive-real axis or in the fourth quadrant of the  $k_\rho$ –plane, with residues  $R_i$  determined according to Table 4. There

<sup>35</sup>Note that, unlike the poles, the residues depend on  $z$  and  $z'$ .

Table 4: Relationship between kernel residues and TLGF residues.

Kernel	$R_i^e$	$R_i^h$
$G_0$	$-R_{1i}^e/(k_{\rho i}^e)^2$	$R_{1i}^h/(k_{\rho i}^h)^2$
$G_1$	N/A	$R_{1i}^h$
$G_2^a$	$[A - B/(k_{\rho i}^e)^2] R_{2i}^e$	$B R_{2i}^h/(k_{\rho i}^h)^2$
$G_3$	$-\mu_{tm} R_{3i}^e$	$\mu_{tm} R_{3i}^h$
$G_4$	$-\mu_{tn} R_{4i}^e$	$\mu_{tn} R_{4i}^h$
$G_5$	$R_{1i}^e$	$R_{1i}^h$
$G_6$	$-R_{1i}^e$	$R_{1i}^h$
$G_7$	$R_{4i}^e/\epsilon_{zn}$	N/A
$G_8$	$R_{3i}^e/\epsilon_{zm}$	N/A
$G_9$	$R_{2i}^e (k_{\rho i}^e)^2 / (\epsilon_{zn} \epsilon_{zm})$	N/A
$G_{11}$	$-R_{4i}^e$	$R_{4i}^h$
$G_{12}$	$R_{4i}^e$	$R_{4i}^h$
$G_{13}$	N/A	$R_{1i}^h/\mu_{zn}$
$G_{14}$	$R_{2i}^e/\epsilon_{zm}$	N/A

---


$$^a A = \mu_{tm}/\epsilon_{zn} + \mu_{tn}/\epsilon_{zm}, \quad B = \mu_{tm}\mu_{tn}$$

is no need here to distinguish between the poles and residues of the TM and TE types, as they are treated in the same fashion. The guided-wave part of this kernel will have the form

$$\tilde{G}^p = \sum_{i=1}^{N_p} \left( \frac{2R_i k_{\rho i}}{k_\rho^2 - k_{\rho i}^2} - \frac{2R_i k_{\rho i}}{k_\rho^2 + k_{\rho i}^2} \right) = \sum_{i=1}^{N_p} \frac{4R_i k_{\rho i}^3}{k_\rho^4 - k_{\rho i}^4}, \quad (144)$$

where for each pole pair  $\pm k_{\rho i}$ , we also include a spurious, non-existent pole pair  $\mp j k_{\rho i}$ , as illustrated in Fig. 7. The inclusion of the spurious pole pairs makes the guided-wave expression (144)

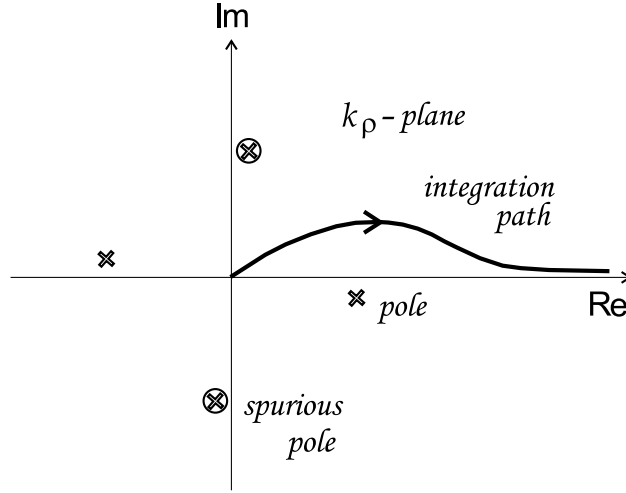


Figure 7: True and spurious pole-pairs.

more rapidly convergent for  $k_\rho \rightarrow \infty$  [50, 51].

The space-domain counterparts of (144) can be obtained by using the integral identities listed in Appendix B. Note that in these identities the terms associated with the spurious poles cancel the undesirable singularities as  $\rho \rightarrow 0$  [5, 52, 53].

### 6.3 Extraction of branch-point terms

In this section, we derive approximate expressions for the branch point (continuous spectrum) contribution to the kernels of a multilayer. The branch point singularities of the spectral domain kernels are associated with half-space media. Hence, let  $k_b$  be the wavenumber of the upper or lower half-space. We assume that there are no other branch points nearby, but allow for the possibility of a pole  $k_p$  arbitrarily close to  $k_b$ , as illustrated in Fig. 8. The location of the pole  $k_p$  and its residue,  $R_p$ , can be determined by the methods of Sec. 6.2. The branch point extraction is only critical for lossless (or near-lossless) half-spaces, since otherwise the associated lateral waves decay rapidly with horizontal distance along the interface.

We consider kernels of the form

$$G(\rho) = \frac{1}{2\pi} \int_0^\infty \tilde{G}(k_\rho) J_n(k_\rho \rho) k_\rho^{n+1} dk_\rho \quad (145)$$

$$= \frac{1}{4\pi} \int_{\infty e^{-j\pi}}^\infty \tilde{G}(k_\rho) H_n^{(2)}(k_\rho \rho) k_\rho^{n+1} dk_\rho, \quad n = 0, 1, 2, \quad (146)$$

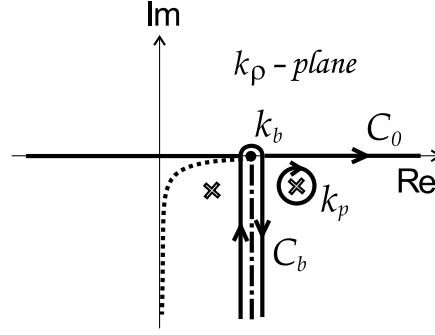


Figure 8: Original and deformed integration paths in  $k_\rho$ -plane.

where  $\tilde{G}$  is an even function of  $k_\rho$ . The integration path in (146) is along the real axis and is illustrated as path  $C_0$  in Fig. 8. The inverse Hankel transform of (145) gives

$$\tilde{G}(k_\rho) = 2\pi k_\rho^{-n} \int_0^\infty G(\rho) J_n(k_\rho \rho) \rho d\rho. \quad (147)$$

For simplicity, we do not indicate the dependence of the kernels on  $z$  and  $z'$ , which are assumed to have fixed values.

The branch point at  $k_b$  arises because  $\tilde{G}$  is not an even function of  $k_{zb} = \sqrt{k_b^2 - k_\rho^2}$ . The hyperbolic branch cut emanating from  $k_b$ , as illustrated in Fig. 8, delineates the boundary along  $\Im k_{zb} = 0$  between the proper ( $\Im k_{zb} < 0$ ) and improper ( $\Im k_{zb} > 0$ ) sheets of the Riemann surface associated with  $k_{zb}$  [54, p. 610]. The real axis integration path  $C_0$  may be deformed to the path  $C_b$ , wrapped around a vertical semi-infinite line emanating from the branch point  $k_b$ , as illustrated in Fig. 8. Note that the left segment of  $C_b$  lies on the improper sheet and the right segment lies on the proper sheet. The modified integral must be augmented by the contributions from the singularities captured in the path deformation process, including proper and improper poles and possibly another branch point. Assuming large  $\rho$ , the integral along  $C_b$  may be approximated as

$$G^b(\rho) = \frac{1}{4\pi} \int_{C_b} \tilde{G}(k_\rho) H_n^{(2)}(k_\rho \rho) k_\rho^{n+1} dk_\rho, \quad (148)$$

$$\approx \frac{1}{4\pi} \sqrt{\frac{2j}{\pi\rho}} j^n \int_{C_b} \tilde{G}(k_\rho) e^{-jk_\rho \rho} k_\rho^{n+1/2} dk_\rho, \quad (149)$$

where we have used the asymptotic form of the Hankel function [26, eq. 9.2.4]. It can be shown that there is no contribution to the integral from the semi-circular arc of vanishing radius passing above  $k_b$  [55, p. 157]. The remainder of  $C_b$  follows the steepest descent path away from the branch point [21, p. 430] and the integration along this path is facilitated by introducing a new variable  $s$  as

$$k_\rho = k_b - js^2, \quad s = e^{j\pi/4} \sqrt{k_\rho - k_b}. \quad (150)$$

Clearly, the integrand falls off rapidly with increasing  $s$  and most of the contribution to the integral comes from the vicinity of the branch point  $k_\rho = k_b$ , where  $s$  and  $k_{zb} \approx \pm s(1+j)\sqrt{k_b}$  are small. Hence, we may further approximate (149) as

$$G^b(\rho) \approx \frac{1}{\pi} \frac{j^n k_b^{n+1/2}}{\sqrt{2\pi j\rho}} e^{-jk_b \rho} \int_0^\infty [\tilde{G}^+(s) - \tilde{G}^-(s)] e^{-s^2 \rho} s ds. \quad (151)$$

Here,  $\tilde{G}(s)$  stands for  $\tilde{G}(k_\rho)$  with  $k_\rho$  given by the first expression in (150). The superscript ‘+’ (‘−’) indicates that the kernel should be evaluated on the proper (improper) Riemann sheet. The integration path in (151) is the positive-real semi-axis in the  $s$ –plane, as illustrated in Fig. 9, where we also show the  $s$ –plane image of the path  $C_0$  and the mapping of the poles from Fig. 8.

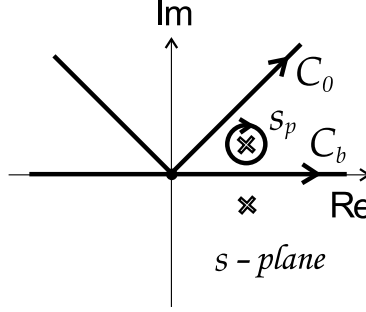


Figure 9: Integration paths in  $s$ –plane.

Since  $\tilde{G}^-$  is  $\tilde{G}^+$  with the proper sheet value of  $k_{zb}$  replaced by  $-k_{zb}$ , the difference of  $\tilde{G}^+$  and  $\tilde{G}^-$  in (151) is an odd function of  $k_{zb}$ , and thus an odd function of  $s$ . Hence, in the vicinity of the branch point we may use the approximation (cf. [56, 57])

$$\tilde{F}(s) \equiv \tilde{G}^+(s) - \tilde{G}^-(s) \approx \frac{Bs}{s^2 - s_p^2}, \quad (152)$$

where  $B$  is a constant coefficient. Assuming that (152) holds, we obtain the relationship

$$R_p = \mp j s_p B, \quad (153)$$

where the upper (lower) sign applies if the pole is on the proper (improper) Riemann sheet. Note that  $s_p = 0$  if the pole coalesces with the branch point, in which case  $R_p = 0$  (but  $B$  remains finite). Hence, the last case excepted,  $B$  could be obtained from the residue  $R_p$ , but the value may be inaccurate if the pole is far away from the branch point. For two-layer media, it is not difficult to derive analytical expressions for  $B$  by expanding the kernel about  $k_{zb} = 0$ , but this procedure can become cumbersome for the general case of multilayered media [50]. Here, we have opted for a simple least-squares fitting procedure, similar to that previously used by Boix et al. [57].<sup>36</sup> Hence, by enforcing (152) at a sequence of points  $s_i, i = 1, 2, \dots, M$ , along the real axis near the branch point  $s = 0$ , we find  $B$  as

$$B = \frac{\sum_{i=1}^M \tilde{F}(s_i)(s_i^2 - s_p^2)s_i}{\sum_{i=1}^M s_i^2}, \quad (154)$$

where the number of points  $M$  and the sampling interval are not critical. Usually, good results are obtained with  $M = 50$  and  $s_i$  uniformly distributed in the range  $0 < s_i < 0.001\sqrt{k_0}$ .

With  $B$  thus determined, we can use (152) in (151), to obtain

$$G^b(\rho) \approx \frac{1}{2\pi} \frac{B j^n k_b^{n+1/2}}{(1+j)\sqrt{\pi\rho}} e^{-jk_b\rho} \int_{-\infty}^{\infty} e^{-s^2\rho} \frac{s^2 ds}{s^2 - s_p^2}, \quad (155)$$

<sup>36</sup>These authors use the least-squares fitting to determine both  $s_p$  and  $B$ , and then compute  $R_p$  from (153).

where the integration has been extended to the entire real axis in Fig. 9. Simple, closed-form, approximate expressions for the integral in (155) can be derived for two limiting cases, where  $|s_p|^2\rho$  is either small or large, and thus either  $s_p^2$  or  $s^2$  may be neglected, respectively, in the denominator of the integrand. As a result, we obtain

$$G^b(\rho) \approx \frac{1}{2\pi} \frac{Bj^n k_b^{n+1/2}}{(1+j)\rho} e^{-jk_b\rho} \begin{cases} 1 & \text{if } |s_p|^2\rho \rightarrow 0, \\ -\frac{1}{2s_p^2\rho} & \text{if } |s_p|^2\rho \rightarrow \infty. \end{cases} \quad (156)$$

The two approximations in (156) can be stitched together by means of suitable exponential transition functions dependent on the ‘numerical distance’  $s_p^2\rho$  [57]. Also, the undesirable singularity at  $\rho = 0$  can be annihilated by introducing another exponential factor [50, 58]. After these modifications, we arrive at

$$G^b(\rho) = \frac{1}{2\pi} \frac{Bj^n k_b^{n+1/2}}{1+j} e^{-jk_b\rho} \frac{(1 - e^{-k_0\rho})}{\rho} \left[ e^{-|s_p|^2\rho} - \frac{(1 - e^{-|s_p|^2\rho})}{2s_p^2\rho} \right], \quad (157)$$

which is applicable for all values of  $\rho$ . This expression is recognized as the ‘residual wave’ previously derived by Boix et al. [57] in the context of their enhanced total least-squares method. Note that the transition functions make the first or the second term in the brackets dominate, depending on the magnitude of the numerical distance. Hence,  $G^b(\rho)$  is initially  $\mathcal{O}(\rho^{-1})$ , but it becomes  $\mathcal{O}(\rho^{-2})$  for sufficiently large  $\rho$ , with a phase delay  $k_b\rho$ . Therefore, despite the crude approximations involved, the expression (157) exhibits the most important characteristics associated with a branch point wave (also called a lateral wave) when the horizontal distance between the source and the observation point is large [50], [54, p. 464].

Returning to (155), we may also express it as

$$G^b(\rho) \approx \frac{1}{2\pi} \frac{Bj^n k_b^{n+1/2}}{(1+j)\rho} e^{-jk_b\rho} \left( 1 + s_p^2 \sqrt{\frac{\rho}{\pi}} \int_{-\infty}^{\infty} \frac{e^{-s^2\rho}}{s^2 - s_p^2} ds \right), \quad (158)$$

where we used the substitution

$$\frac{s^2}{s^2 - s_p^2} = 1 + \frac{s_p^2}{s^2 - s_p^2}. \quad (159)$$

The integral in (158), which will be denoted by  $I_p$ , can be evaluated as (cf. [21, Sec. 4.4], [59, Sec. 27.2], [60])

$$I_p = \pm \frac{2j}{s_p} \sqrt{\pi} e^{-s_p^2\rho} Q(\mp j s_p \sqrt{\rho}), \quad \Im s_p \geq 0, \quad (160)$$

where

$$Q(z) = \int_z^{\infty} e^{-t^2} dt \quad (161)$$

is proportional to the error function complement,  $\text{erfc}$  [26, Eq. 7.1.2]. The upper or lower sign is selected in (160) depending on whether the pole lies above or below the positive-real axis in Fig. 9,

and the two expressions differ by the residue of the integrand at the pole.<sup>37</sup> Upon substituting (160) into (158), we finally obtain

$$G^b(\rho) \approx \frac{1}{2\pi} \frac{Bj^n k_b^{n+1/2}}{(1+j)\rho} e^{-jk_b\rho} \left[ 1 \pm 2js_p\sqrt{\rho} e^{-s_p^2\rho} Q(\mp js_p\sqrt{\rho}) \right], \quad \Im s_p \geq 0. \quad (162)$$

Although this expression is applicable for all (sufficiently large) values of  $\rho$ , it does not have a closed-form spectral domain counterpart. To remedy this, we may try using the asymptotic expansion [21, p. 405]<sup>38</sup>

$$\pm 2js_p\sqrt{\rho} e^{-s_p^2\rho} Q(\mp js_p\sqrt{\rho}) \sim - \left( 1 + \frac{1}{2s_p^2\rho} + \dots \right), \quad |s_p|^2\rho \rightarrow \infty, \quad (163)$$

which, however, leads back to (156).

Hence, we adopt for  $G^b$  the expression (157). Its spectral domain counterpart,  $\tilde{G}^b$ , is obtained by applying the inverse Hankel transform (147). The integration can be done in closed form by invoking [61, p. 386]. The result depends on the order  $n$  of the transform, and is given as

$$\tilde{G}^b(k_\rho) = \frac{Bj^n k_b^{n+1/2}}{1+j} \left[ I_n^{(1)} - \frac{1}{2s_p^2} I_n^{(2)} \right], \quad (164)$$

with

$$I_n^{(1)} = \left[ \frac{\left( \sqrt{k_\rho^2 + c^2} + c \right)^{-n}}{\sqrt{k_\rho^2 + c^2}} - \frac{\left( \sqrt{k_\rho^2 + d^2} + d \right)^{-n}}{\sqrt{k_\rho^2 + d^2}} \right], \quad n = 0, 1, 2, \quad (165)$$

and

$$I_n^{(2)} = \begin{cases} \ln \left[ \frac{\left( \sqrt{k_\rho^2 + b^2} + b \right) \left( \sqrt{k_\rho^2 + c^2} + c \right)}{\left( \sqrt{k_\rho^2 + a^2} + a \right) \left( \sqrt{k_\rho^2 + d^2} + d \right)} \right], & n = 0, \\ \frac{1}{n} \left[ \left( \sqrt{k_\rho^2 + a^2} + a \right)^{-n} - \left( \sqrt{k_\rho^2 + b^2} + b \right)^{-n} \right. \\ \left. - \left( \sqrt{k_\rho^2 + c^2} + c \right)^{-n} + \left( \sqrt{k_\rho^2 + d^2} + d \right)^{-n} \right], & n = 1, 2, \end{cases} \quad (166)$$

where the notation given in Table 5 is used.<sup>39</sup> The asymptotic behavior of (164) is no worse than  $\mathcal{O}(k_\rho^{-3})$ .

<sup>37</sup>When the pole is on the real axis ( $\Im s_p = 0$ ), (160) must be properly modified by one-half of the residue [21, p. 399], [60].

<sup>38</sup>Note that the expressions corresponding to the upper and lower signs are asymptotically equivalent. This is because the residue term of the integrand of  $I_p$  at the pole  $s_p$  vanishes exponentially for large  $\rho$ .

<sup>39</sup>The upper expression in (166) was obtained by letting  $n \rightarrow 0$  in the lower expression.

Table 5: Notation used in the expression for  $\tilde{G}^b$ .

$a$	$b$	$c$	$d$
$jk_b$	$a + k_0$	$a +  s_p ^2$	$b +  s_p ^2$

## 6.4 Exponential fit

Consider now a remainder kernel of the form

$$\tilde{G}^c = \tilde{G} - \tilde{G}^q - \tilde{G}^p, \quad (167)$$

which applies to all kernels except  $G_6$  and  $G_9$ , for which the quasi-static term  $\tilde{G}^q$  must be multiplied by  $(k_\rho/k_0)^2$ . In the above,  $\tilde{G}^q$  is given by one of the three forms (140)–(141) and  $\tilde{G}^p$  is given by (144). The exponential fit of  $\tilde{G}^c$  can be obtained by the matrix pencil method (MPM) [62, 63], which is based on uniform sampling along a suitable linear path in the complex  $k_{zq}$ -plane. The robustness of the DCIM can be improved by the recursive application of the MPM on two or three piecewise-linear path segments, which can have different lengths and sampling rates [40, 64]. We use a two-level approach, with the sampling paths illustrated in Fig. 10. The path segments  $C_l$ ,  $l = 1, 2$ , in the  $k_{zq}$ -plane are parameterized in terms of a real parameter  $t$  as

$$k_{zq} = \gamma_{l-1} + (\gamma_l - \gamma_{l-1})t, \quad 0 \leq t < 1, \quad (168)$$

with<sup>40</sup>

$$\gamma_0 \equiv k_q, \quad \gamma_l = \sqrt{k_q^2 - \kappa_l^2}, \quad (169)$$

where  $k_q = k_0 n_q$  is the wavenumber of the “equivalent medium” introduced in Sec. 6.1. In the last expression, the square root branch with non-positive imaginary part is implied. The corresponding path in the  $k_\rho$ -plane is given by the mapping (108). The values of  $\kappa_1$  and  $\kappa_2$  are selected first, to ensure desirable path properties in the  $k_\rho$ -plane, and they determine the location of  $\gamma_1$  and  $\gamma_2$  via (169). Here, we choose

$$\kappa_1/k_0 = \max \Re n_{\text{eff},n}^\alpha + 1, \quad (170)$$

to ensure that the kernel singularities (guided-wave poles and branch points) located near the real axis are avoided. The value of  $\kappa_2/k_0$  is less critical and is typically set to a number two orders of magnitude greater than  $\kappa_1/k_0$ .

In the two-level DCIM approach, we first apply the MPM on  $C_2$ , which results in

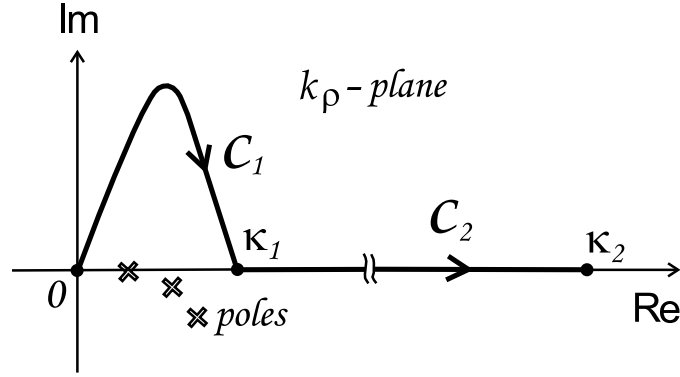
$$jk_{zq}\tilde{G}^c \approx \sum_{i=1}^{N_2} \alpha_{2i} e^{\beta_{2i}t} = \sum_{i=1}^{N_2} a_{2i} e^{-jk_{zq}b_{2i}}. \quad (171)$$

Next, we subtract the so obtained exponential fit from the original function and apply the MPM to the remainder function on  $C_1$  as

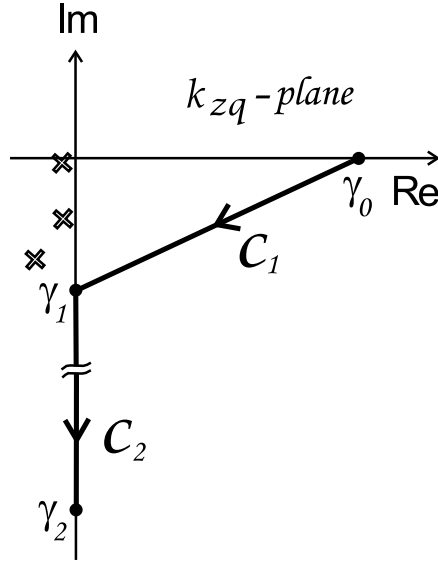
$$jk_{zq}\tilde{G}^c - \sum_{i=1}^{N_2} a_{2i} e^{-jk_{zq}b_{2i}} \approx \sum_{i=1}^{N_1} \alpha_{1i} e^{\beta_{1i}t} = \sum_{i=1}^{N_1} a_{1i} e^{-jk_{zq}b_{1i}}. \quad (172)$$

<sup>40</sup>The symbol  $\kappa$  used here is unrelated to the same symbol introduced before in (105).





(a)



(b)

Figure 10: DCIM sampling paths in (a)  $k_\rho$ -plane and (b)  $k_{zq}$ -plane.

On each level  $l$ , the MPM automatically determines the number of exponential terms,  $N_l$ , based on the specified precision of the samples (i.e., an estimate of the number of significant digits in the data), and returns the coefficients  $\alpha_{li}$  and  $\beta_{li}$ . From the latter, using the mapping (168), the coefficients  $a_{li}$  and  $b_{li}$  are found as

$$b_{li} = \frac{j\beta_{li}}{\gamma_l - \gamma_{l-1}}, \quad a_{li} = \alpha_{li} e^{j\gamma_{l-1}b_{li}}. \quad (173)$$

As a result of these steps, we finally obtain the approximation

$$\tilde{G}^c \approx \sum_{l=1}^L \sum_{i=1}^{N_l} a_{li} \frac{e^{-jk_{zq}b_{li}}}{jk_{zq}}, \quad (174)$$

with the number of levels  $L = 2$ . In the above, the exponential fit was applied to  $j k_{zq} \tilde{G}^c$ , but it is

also possible to apply it directly to  $\tilde{G}^c$ , which leads to

$$\tilde{G}^c \approx \sum_{l=1}^L \sum_{i=1}^{N_l} a_{li} e^{-jk_{zq} b_{li}}. \quad (175)$$

We use the former procedure for kernels  $G_0, G_1, G_2, G_5, G_6, G_9, G_{13}$ , and  $G_{14}$ , and the latter for kernels  $G_3, G_4, G_7, G_8, G_{11}$ , and  $G_{12}$ .

We refer to (174) and (175) as complex image approximations. The closed-form space-domain counterparts of these expressions can be obtained by using the appropriate integral identities from among those listed in Appendix A. If desired, the two-level approach described above can easily be reduced to a one-level approach ( $L = 1$ ), where the MPM is only applied on the path segment  $C_1$ , or extended to a three-level method ( $L = 3$ ), where a third path segment is appended to the sampling path of Fig. 10.<sup>41</sup>

In the case of  $G_0, G_1$ , and  $G_2$ , the above procedure results in<sup>42</sup>

$$G(\rho) = \frac{1}{2\pi} \left\{ \sum_{i=1}^{N_q} a_{qi} \frac{e^{-jk_q r_{qi}}}{r_{qi}} + \sum_{l=1}^L \sum_{i=1}^{N_l} a_{li} \frac{e^{-jk_q r_{li}}}{r_{li}} + \sum_{i=1}^{N_p} (-2R_i k_{\rho i}) \left[ \frac{j\pi}{2} H_0^{(2)}(k_{\rho i} \rho) + K_0(k_{\rho i} \rho) \right] \right\}, \quad (176)$$

with

$$r_{\delta i} = \sqrt{\rho^2 + b_{\delta i}^2}, \quad \delta = q, l, \quad (177)$$

where the square root branch with positive real part is selected. In the above, we applied identities (186) and (202) to the quasi-static and complex image terms, respectively.

In the case of  $G_3$  and  $G_4$ , we arrive at

$$G(\rho) = \frac{1}{2\pi} \left\{ \sum_{i=1}^{N_q} \frac{a_{qi}}{\rho} \left( e^{-jk_q b_{qi}} - \frac{b_{qi}}{r_{qi}} e^{-jk_q r_{qi}} \right) + \sum_{l=1}^L \sum_{i=1}^{N_l} \frac{a_{li}}{\rho} \left( e^{-jk_q b_{li}} - \frac{b_{li}}{r_{li}} e^{-jk_q r_{li}} \right) + \sum_{i=1}^{N_p} (-2R_i) \left[ \frac{j\pi}{2} H_1^{(2)}(k_{\rho i} \rho) - K_1(k_{\rho i} \rho) + \frac{2}{k_{\rho i} \rho} \right] \right\}. \quad (178)$$

Here, the quasi-static and complex image terms were inverted by (191), and the guided-wave terms by (203).

<sup>41</sup>Extensive numerical experiments (not reported here) have shown that the three-level approach can exhibit erratic behavior, and is thus unreliable.

<sup>42</sup>Henceforth, we write  $G(\rho)$  rather than  $G(\rho; z|z')$ , to emphasize that the kernels are closed-form, as far as the  $\rho$ -dependence is concerned. The dependence on  $z$  and  $z'$  is implicit in the quasi-static and complex-image coefficients, and in the pole residues.

In the case of  $G_5$ , we obtain

$$\begin{aligned}
G(\rho) = \frac{1}{2\pi} \left\{ \sum_{i=1}^{N_{q1}} a_{q1i} \left[ \left( \frac{3b_{q1i}^2}{r_{q1i}^2} - 1 \right) (1 + jk_q r_{q1i}) - k_q^2 b_{q1i}^2 \right] \frac{e^{-jk_q r_{q1i}}}{r_{q1i}^3} \right. \\
+ \sum_{i=1}^{N_{q2}} a_{q2i} \frac{e^{-jk_q r_{q2i}}}{r_{q2i}} + \sum_{l=1}^L \sum_{i=1}^{N_l} a_{li} \frac{e^{-jk_q r_{li}}}{r_{li}} \\
\left. + \sum_{i=1}^{N_p} (-2R_i k_{\rho i}) \left[ \frac{j\pi}{2} H_0^{(2)}(k_{\rho i} \rho) + K_0(k_{\rho i} \rho) \right] \right\}, \quad (179)
\end{aligned}$$

where  $r_{qki}$ ,  $k = 1, 2$ , is given by (177), with  $k$  added to the subscript list. In the above, the quasi-static terms were inverted by (188) and (186), the complex-image terms by (186), and the guided-wave terms by (202).

In the case of  $G_6$ , we obtain

$$\begin{aligned}
G(\rho) = \frac{1}{2\pi} \left\{ \sum_{i=1}^{N_q} a_{qi} \left[ \frac{3\rho^2}{r_{qi}^2} (1 + jk_q r_{qi}) - k_q^2 \rho^2 \right] \frac{e^{-jk_q r_{qi}}}{r_{qi}^3} \right. \\
+ \sum_{l=1}^L \sum_{i=1}^{N_l} a_{li} \left[ \frac{2}{jk_q \rho^2} (e^{-jk_q b_{li}} - e^{-jk_q r_{li}}) - \frac{e^{-jk_q r_{li}}}{r_{li}} \right] \\
\left. + \sum_{i=1}^{N_p} (-2R_i k_{\rho i}) \left[ \frac{j\pi}{2} H_2^{(2)}(k_{\rho i} \rho) - K_2(k_{\rho i} \rho) + \frac{4}{(k_{\rho i} \rho)^2} \right] \right\}. \quad (180)
\end{aligned}$$

Here, the quasi-static terms were inverted by (196), the complex image terms by (194), and the guided-wave terms by (205).

In the case of  $G_7$  and  $G_8$ , we obtain

$$\begin{aligned}
G(\rho) = \frac{1}{2\pi} \left\{ \sum_{i=1}^{N_q} a_{qi} \left[ \frac{3b_{qi}\rho}{r_{qi}^2} (1 + jk_q r_{qi}) - k_q^2 b_{qi}\rho \right] \frac{e^{-jk_q r_{qi}}}{r_{qi}^3} \right. \\
+ \sum_{l=1}^L \sum_{i=1}^{N_l} a_{li} \left[ \frac{3b_{li}\rho}{r_{li}^2} (1 + jk_q r_{li}) - k_q^2 b_{li}\rho \right] \frac{e^{-jk_q r_{li}}}{r_{li}^3} \\
\left. + \sum_{i=1}^{N_p} (-2R_i k_{\rho i}^2) \left[ \frac{j\pi}{2} H_1^{(2)}(k_{\rho i} \rho) + K_1(k_{\rho i} \rho) \right] \right\}. \quad (181)
\end{aligned}$$

Here, the quasi-static and complex image terms were inverted by (193), and the guided-wave terms by (204).

In the case of  $G_9$ , we obtain

$$\begin{aligned}
G(\rho) = \frac{1}{2\pi} & \left\{ \sum_{i=1}^{N_q} a_{qi} \left[ \left( \frac{3b_{qi}^2}{r_{qi}^2} - 1 \right) (1 + jk_q r_{qi}) + k_q^2 \rho^2 \right] \frac{e^{-jk_q r_{qi}}}{r_{qi}^3} \right. \\
& + \sum_{l=1}^L \sum_{i=1}^{N_l} a_{li} \frac{e^{-jk_q r_{li}}}{r_{li}} \\
& \left. + \sum_{i=1}^{N_p} (-2R_i k_{\rho i}) \left[ \frac{j\pi}{2} H_0^{(2)}(k_{\rho i} \rho) + K_0(k_{\rho i} \rho) \right] \right\}. \tag{182}
\end{aligned}$$

Here, the quasi-static terms were inverted by (189), the complex image terms by (186), and the guided-wave terms by (202).

In the case of  $G_{11}$ , we obtain

$$\begin{aligned}
G(\rho) = \frac{1}{2\pi} & \left\{ \sum_{i=1}^{N_q} a_{qi} \left[ \frac{2}{\rho^2} \left( e^{-jk_q b_{qi}} - \frac{b_{qi}}{r_{qi}} e^{-jk_q r_{qi}} \right) - b_{qi} (1 + jk_q r_{qi}) \frac{e^{-jk_q r_{qi}}}{r_{qi}^3} \right] \right. \\
& + \sum_{l=1}^L \sum_{i=1}^{N_l} a_{li} \left[ \frac{2}{\rho^2} \left( e^{-jk_q b_{li}} - \frac{b_{li}}{r_{li}} e^{-jk_q r_{li}} \right) - b_{li} (1 + jk_q r_{li}) \frac{e^{-jk_q r_{li}}}{r_{li}^3} \right] \\
& \left. + \sum_{i=1}^{N_p} (-2R_i k_{\rho i}) \left[ \frac{j\pi}{2} H_2^{(2)}(k_{\rho i} \rho) - K_2(k_{\rho i} \rho) + \frac{4}{(k_{\rho i} \rho)^2} \right] \right\}. \tag{183}
\end{aligned}$$

Here, the quasi-static and complex-image terms were inverted by (195), and the guided-wave terms by (205).

In the case of  $G_{12}$ , we obtain

$$\begin{aligned}
G(\rho) = \frac{1}{2\pi} & \left\{ \sum_{i=1}^{N_q} a_{qi} b_{qi} (1 + jk_q r_{qi}) \frac{e^{-jk_q r_{qi}}}{r_{qi}^3} \right. \\
& + \sum_{l=1}^L \sum_{i=1}^{N_l} a_{li} b_{li} (1 + jk_q r_{li}) \frac{e^{-jk_q r_{li}}}{r_{li}^3} \\
& \left. + \sum_{i=1}^{N_p} (-2R_i k_{\rho i}) \left[ \frac{j\pi}{2} H_0^{(2)}(k_{\rho i} \rho) + K_0(k_{\rho i} \rho) \right] \right\}. \tag{184}
\end{aligned}$$

Here, the quasi-static and complex-image terms were inverted by (187), and the guided-wave terms by (202).

Finally, in the case of  $G_{13}$  and  $G_{14}$ , we obtain

$$\begin{aligned}
G(\rho) = \frac{1}{2\pi} \left\{ \sum_{i=1}^{N_q} a_{qi} \rho (1 + j k_q r_{qi}) \frac{e^{-j k_q r_{qi}}}{r_{qi}^3} \right. \\
+ \sum_{l=1}^L \sum_{i=1}^{N_l} a_{li} \rho (1 + j k_q r_{li}) \frac{e^{-j k_q r_{li}}}{r_{li}^3} \\
\left. + \sum_{i=1}^{N_p} (-2R_i k_{\rho i}^2) \left[ \frac{j\pi}{2} H_1^{(2)}(k_{\rho i} \rho) + K_1(k_{\rho i} \rho) \right] \right\}. \quad (185)
\end{aligned}$$

Here, the quasi-static and complex image terms were inverted by (192), and the guided-wave terms by (204).

The extraction of the guided-wave terms is not necessary in the near zone, where it may even adversely affect the accuracy of the complex image approximation [5, 53]. Hence, it may be advantageous to split the  $\rho$ –range of interest into two subranges, with a demarcation point at  $\rho = \rho_s$ , and extract the guided-wave terms only when  $\rho > \rho_s$ . The location of the switch point, which is not critical, may be selected by the condition  $k_0 \rho_s = \pi$ . The drawback of this approach is that two sets of complex images must be extracted whenever the  $\rho$ –range of interest straddles  $\rho_s$ .

In conclusion of this section, we note that DCIM depends on several user-specified parameters that affect the accuracy of the method. In addition to choosing the number of levels—which is usually two, the user must select the end points of the sampling path segments, and for each segment the number of samples and an estimate of the number of significant digits in the data. Hence, the method requires a certain amount of trial-and-error “tuning” before it can be applied with some confidence.

## 7 Sample results

In this section we present sample results for the five-layer grounded stack problem illustrated in Fig. 11. This test structure is similar to that previously used in [5–7, 65], except that we have made some of the layers magnetic, in order to make the test more demanding. The frequency is 30 GHz. The source and field points are at the fixed level  $z' = z = 0.4$  mm, while the horizontal distance between them is varied over five decades in the range  $10^{-3} < k_0 \rho < 10^2$ . To avoid ambiguity, we assume that  $z = z' + 0$ . For this configuration, in Figs. 12 through 25 we compare the DCIM results with the reference data, obtained by the direct integration method of Sec. 5, for the basic kernels  $G_0$  through  $G_{14}$ . The DCIM results are plotted by a solid line and the reference data by a dashed line. In these figures, we also plot the relative error using a dotted line.<sup>43</sup> We used the two-level DCIM with quasi-static term extraction (using 3 dominant terms) and guided-wave term extraction (at 30 GHz, this structure can support three guided waves, two TM and one TE). The DCIM sampling path was specified as follows:  $\kappa_1/k_0$  was set according to (170) and  $\kappa_2/k_0$  was set to 300. The number of samples was 150, and the number of significant digits was 10—the same for both sampling path segments. These DCIM parameters were used for all kernels.

<sup>43</sup>If the relative error is below 1%, we fix the error scale maximum at 1%.

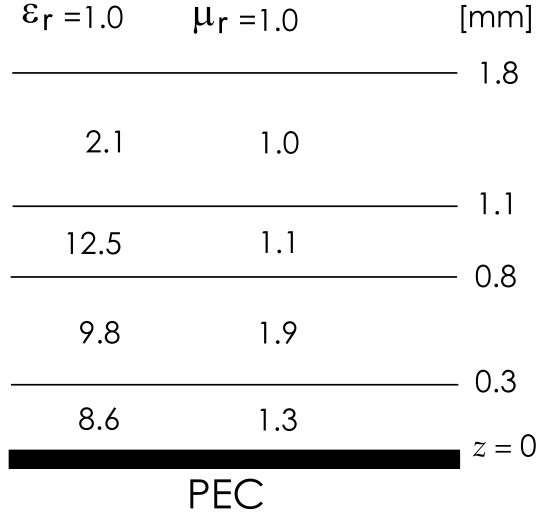


Figure 11: Five-layer stack backed by a PEC groundplane.

The accuracy of these results can be improved by “tuning” the DCIM parameters for each of the kernels individually. Also, the  $\rho$ –switch approach could be implemented to improve the accuracy in the small- $\rho$  range. The slight increase in error observed near the right end of the  $\rho$  range can be attributed to the lateral wave (branch-point contribution) not being accurately sampled in the DCIM.

The results for the dual kernels  $G'_0$  through  $G'_9$  are similar and are omitted to conserve space.

## 8 Conclusion

Insufficient robustness continues to be a problem with the DCIM, even when the quasi-static and guide-wave terms are extracted before the exponential fit is performed. The method can be tuned to yield excellent accuracy for a particular case—or even a particular class of problems, but it can fail, sometimes catastrophically, if some critical parameter of the problem, such as frequency, is changed by an order of magnitude. Increasing the number of sampling levels beyond two does not appear to be a promising remedy. As can be expected, the mildly singular potential kernels are easier to model by the DCIM than the more singular field kernels, especially the hypersingular ones.

The accuracy of the space domain kernels generated by the DCIM is not known a priori and can only be determined by comparisons with the results of other, trusted methods—such as the direct integration method. This appears to be an insurmountable flaw of the DCIM, which may disqualify it as a stand-alone method for critical applications.

The efficiency of the DCIM critically depends on the required number of sampling points, which in turn depends on the spectral behavior of the remainder function (after the quasi-static and guided-wave terms have been extracted) that must be fitted by the complex image representation. The DCIM can be much faster than the direct integration method in cases where  $z$  and  $z'$  are fixed and  $\rho$  is varied, since the coefficients from a single DCIM run (or at most two DCIM runs, if the  $\rho$ –switch is employed) can be reused for different  $\rho$  values.

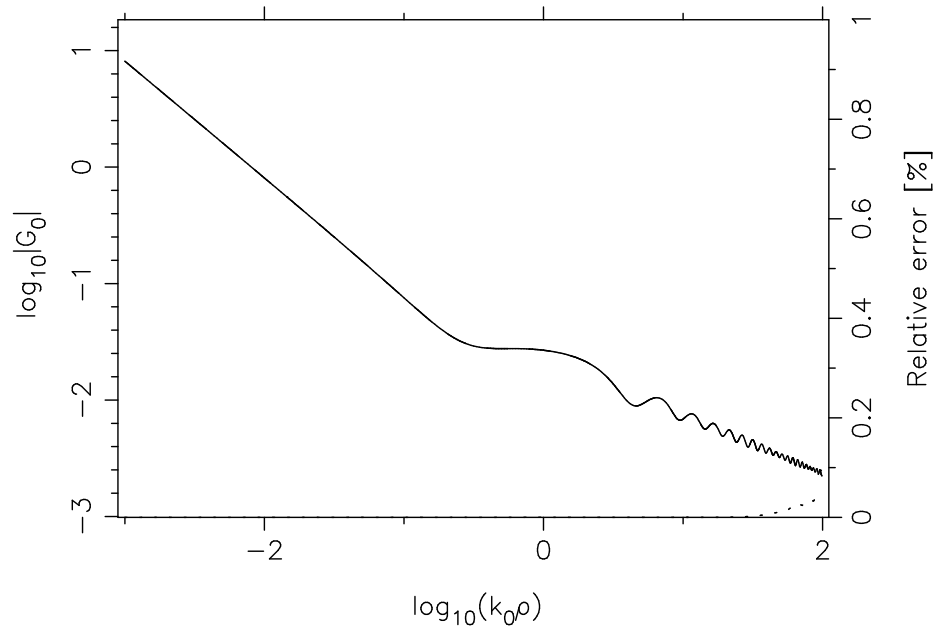


Figure 12: Plot of  $G_0$  vs.  $k_0\rho$  for the problem of Fig. 11 with  $z' = z = 0.4$  mm.

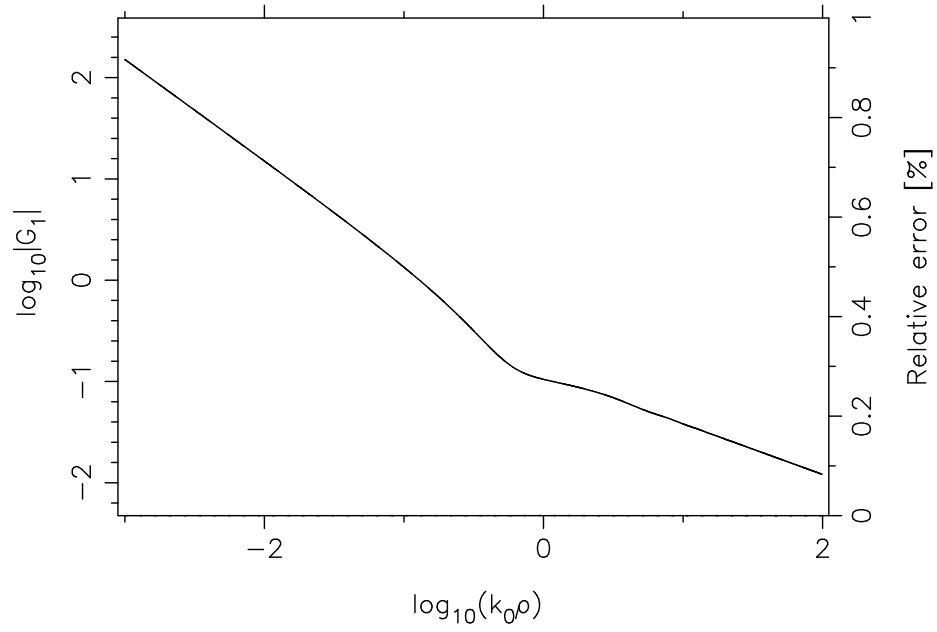


Figure 13: Plot of  $G_1$  vs.  $k_0\rho$  for the problem of Fig. 11 with  $z' = z = 0.4$  mm.

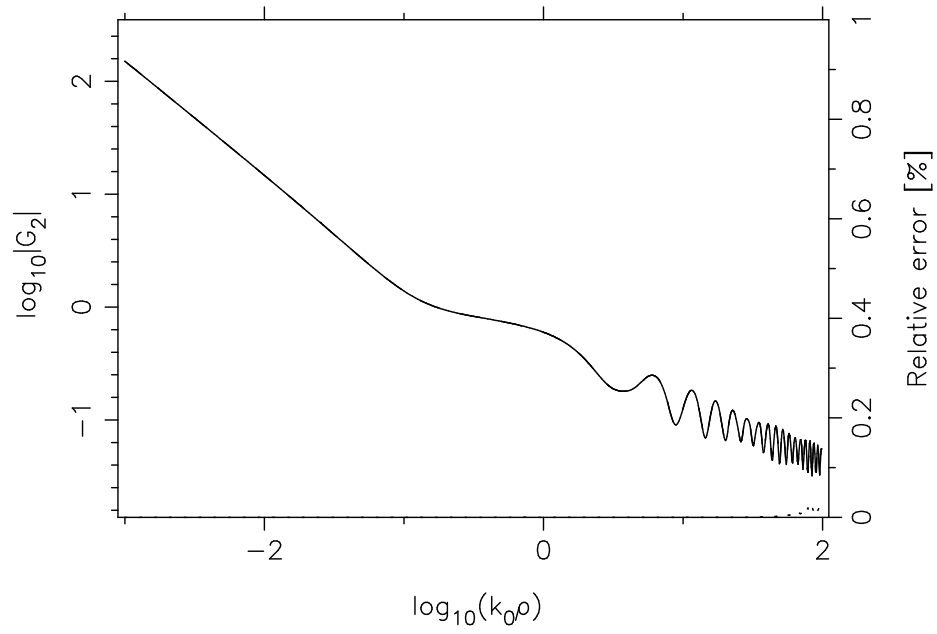


Figure 14: Plot of  $G_2$  vs.  $k_0\rho$  for the problem of Fig. 11 with  $z' = z = 0.4$  mm.

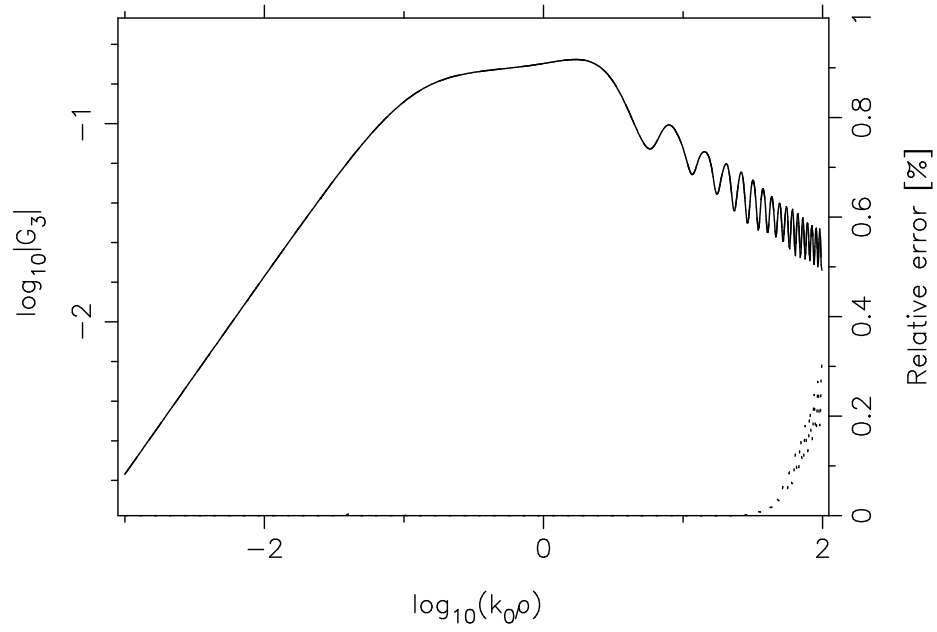


Figure 15: Plot of  $G_3$  vs.  $k_0\rho$  for the problem of Fig. 11 with  $z' = z = 0.4$  mm.



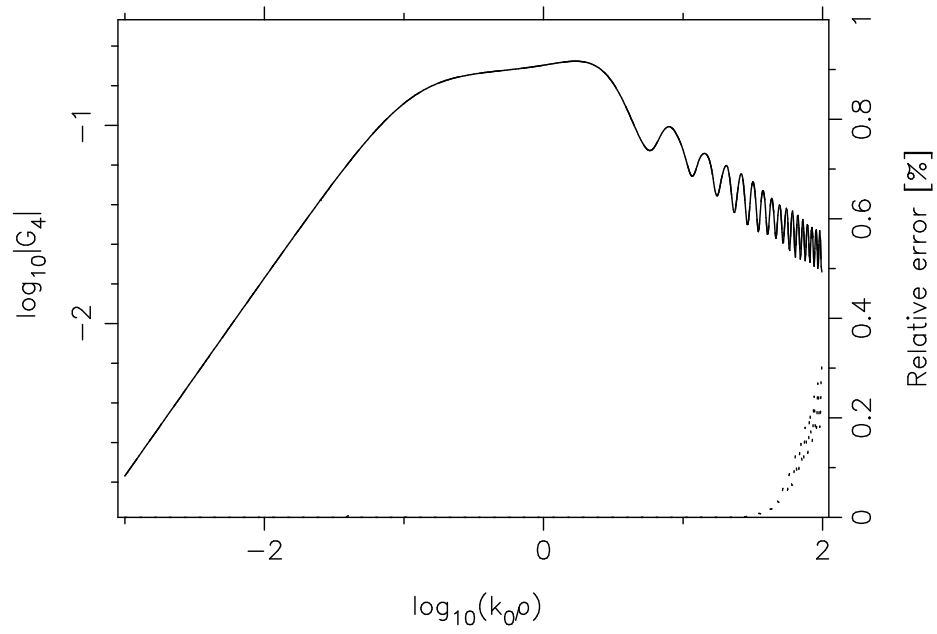


Figure 16: Plot of  $G_4$  vs.  $k_0\rho$  for the problem of Fig. 11 with  $z' = z = 0.4$  mm.

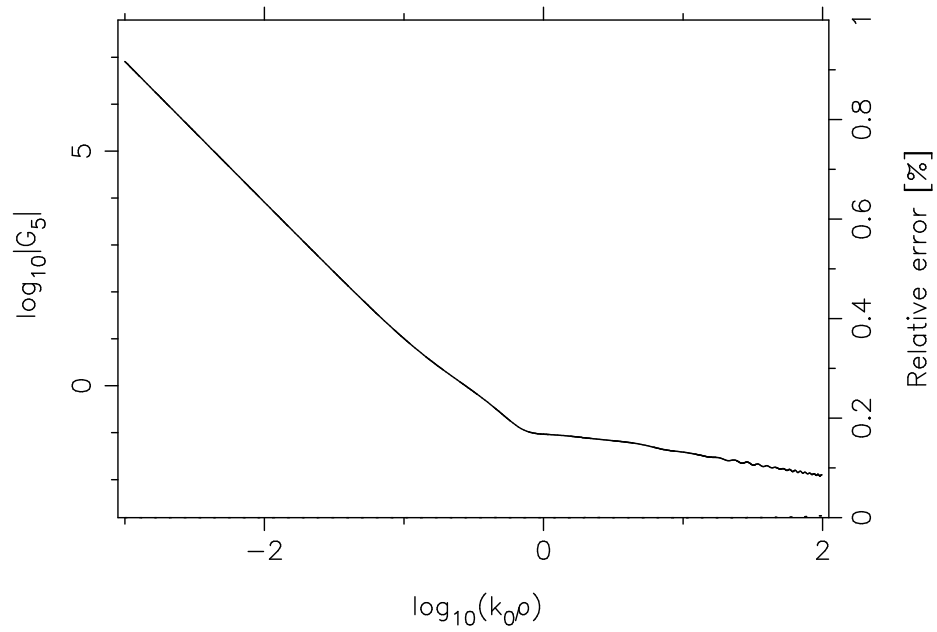


Figure 17: Plot of  $G_5$  vs.  $k_0\rho$  for the problem of Fig. 11 with  $z' = z = 0.4$  mm.

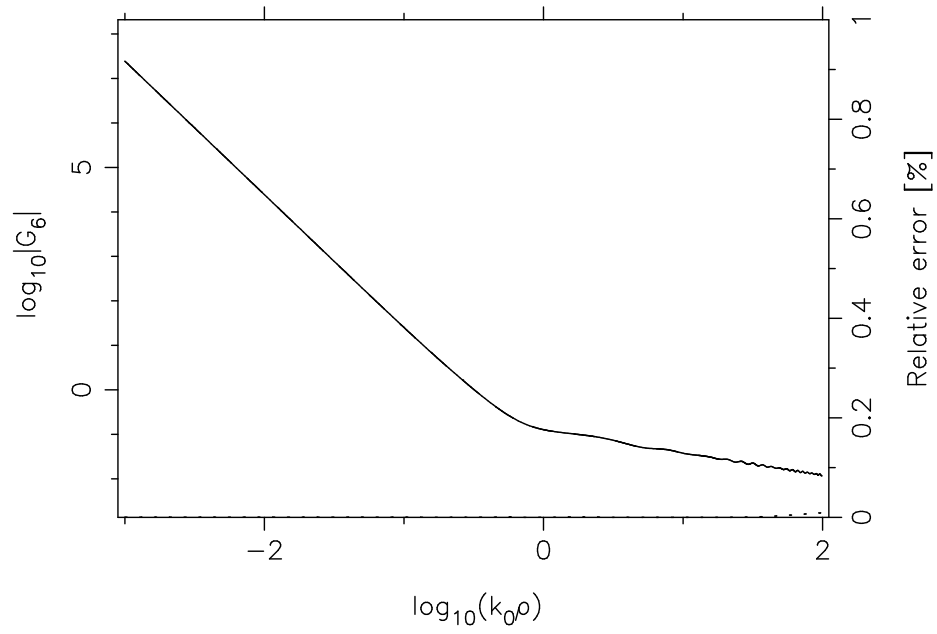


Figure 18: Plot of  $G_6$  vs.  $k_0\rho$  for the problem of Fig. 11 with  $z' = z = 0.4$  mm.

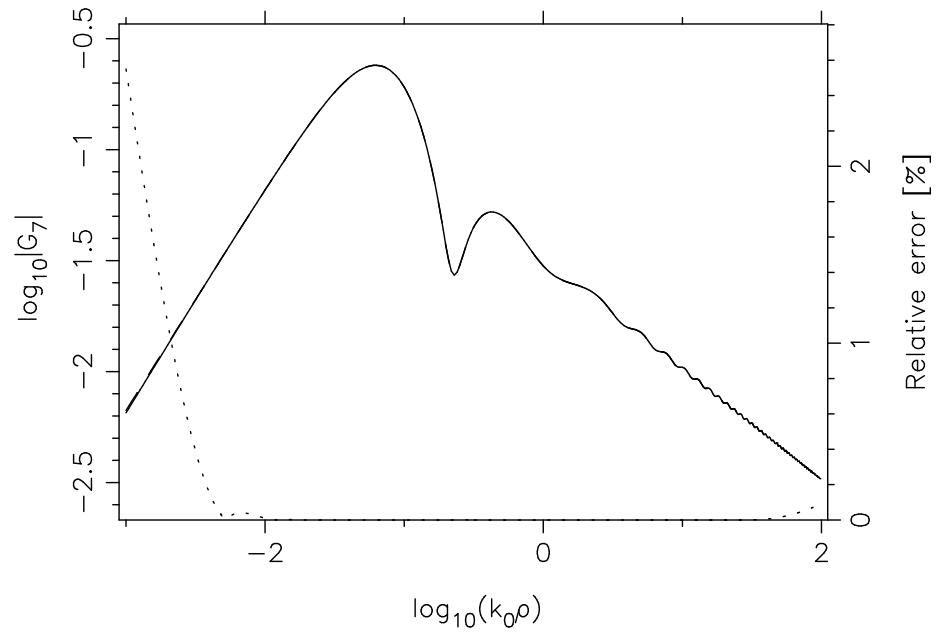


Figure 19: Plot of  $G_7$  vs.  $k_0\rho$  for the problem of Fig. 11 with  $z' = z = 0.4$  mm.

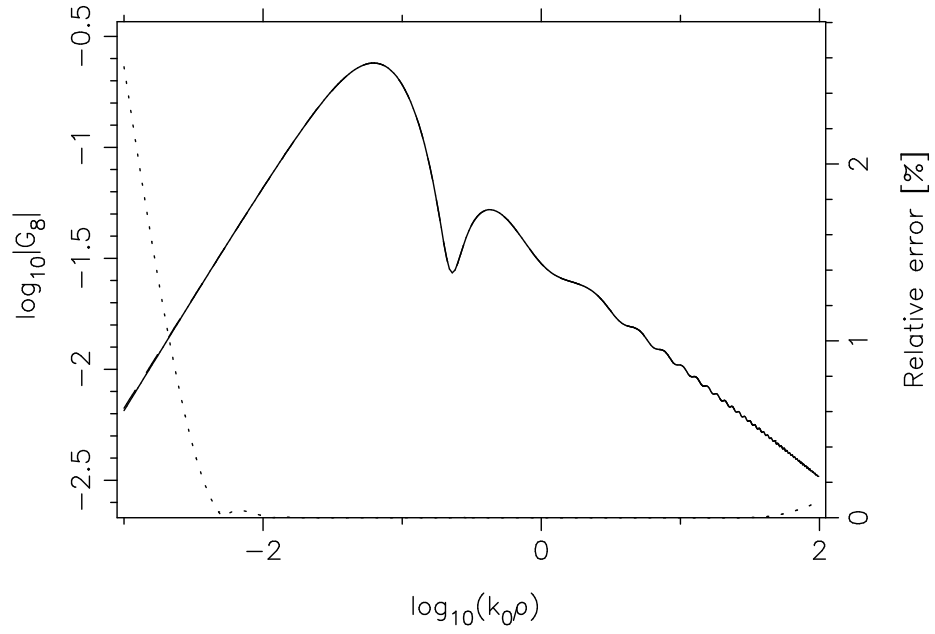


Figure 20: Plot of  $G_8$  vs.  $k_0\rho$  for the problem of Fig. 11 with  $z' = z = 0.4$  mm.

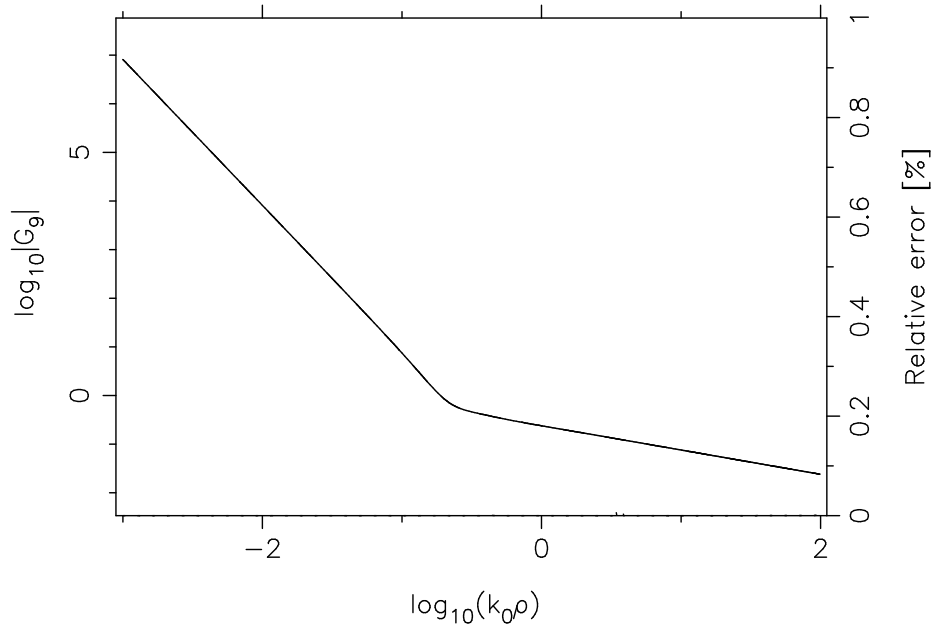


Figure 21: Plot of  $G_9$  vs.  $k_0\rho$  for the problem of Fig. 11 with  $z' = z = 0.4$  mm.

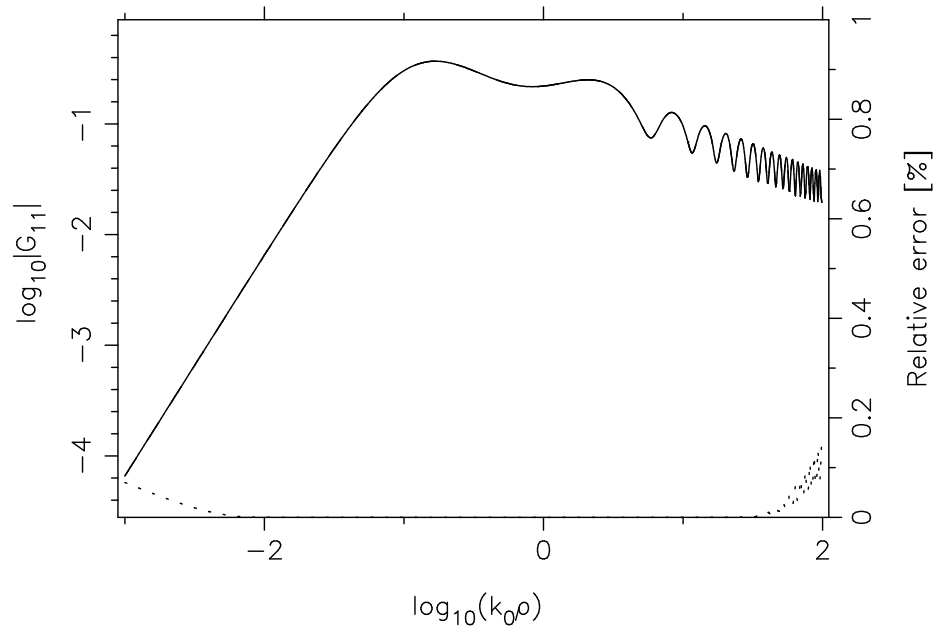


Figure 22: Plot of  $G_{11}$  vs.  $k_0\rho$  for the problem of Fig. 11 with  $z' = z = 0.4$  mm.

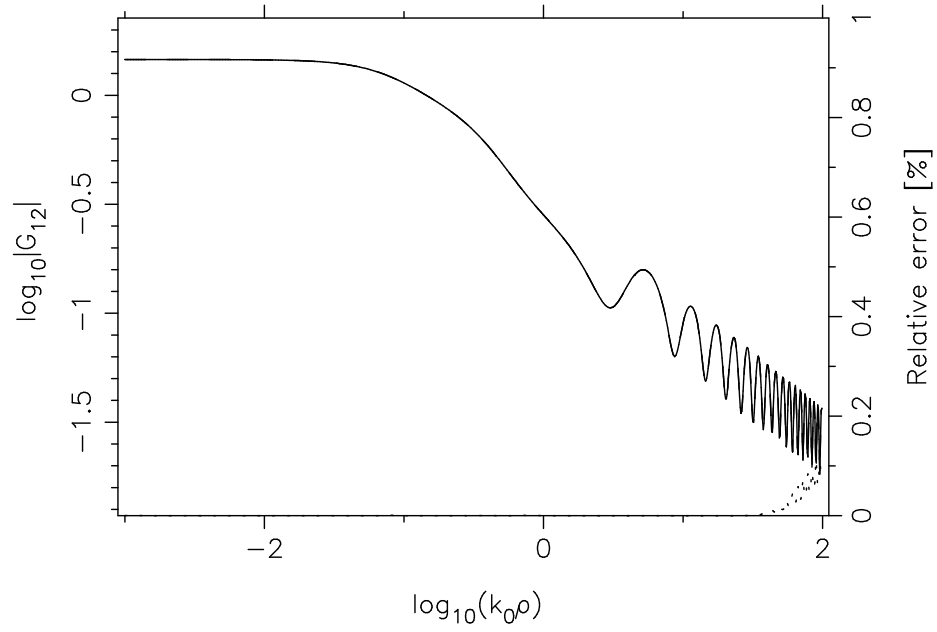


Figure 23: Plot of  $G_{12}$  vs.  $k_0\rho$  for the problem of Fig. 11 with  $z' = z = 0.4$  mm.

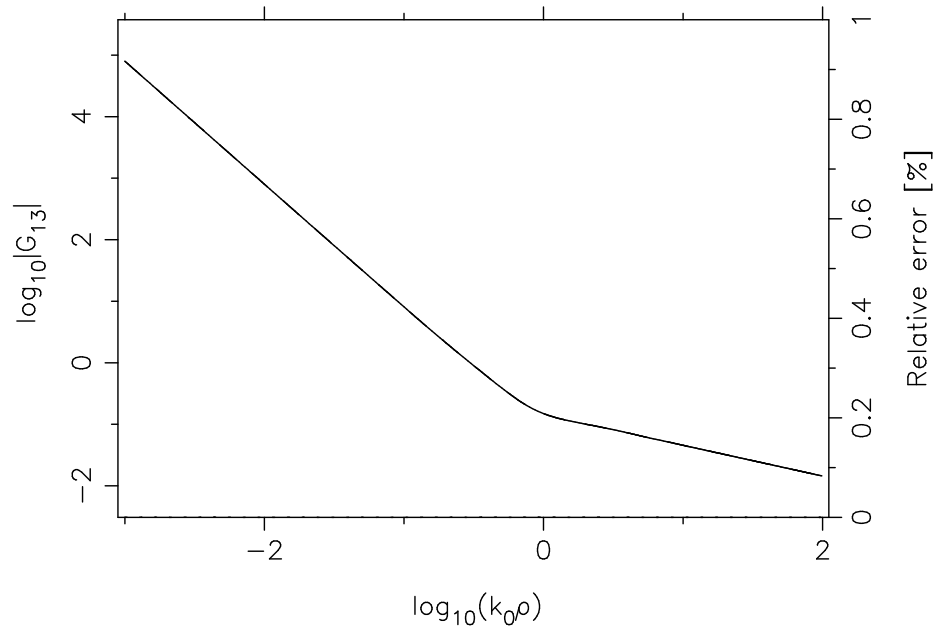


Figure 24: Plot of  $G_{13}$  vs.  $k_0\rho$  for the problem of Fig. 11 with  $z' = z = 0.4$  mm.

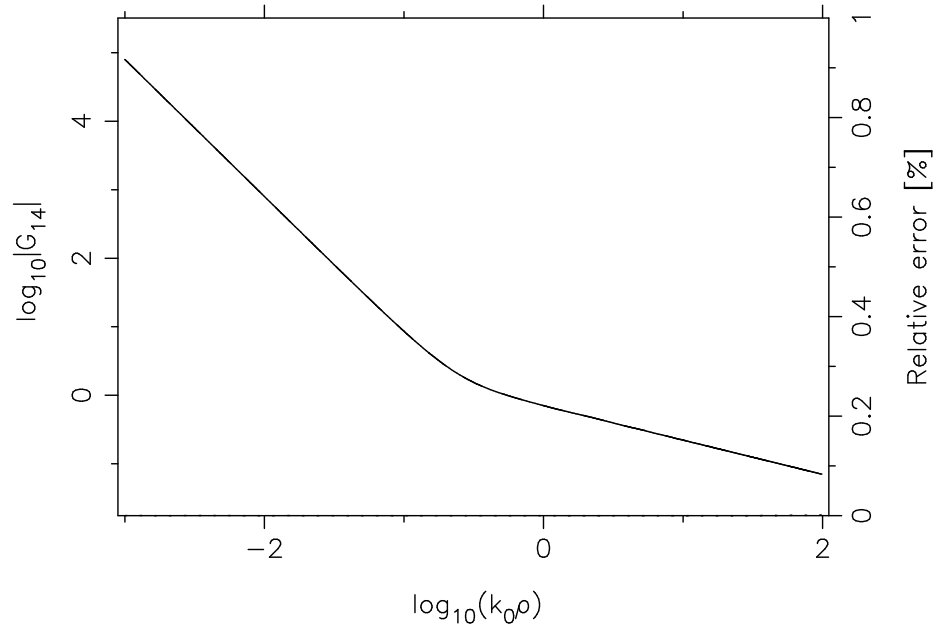


Figure 25: Plot of  $G_{14}$  vs.  $k_0\rho$  for the problem of Fig. 11 with  $z' = z = 0.4$  mm.

Regarding future work, it appears desirable to extract and analytically handle the branch-point contribution to the spectrum, which represents the lateral wave that may propagate unattenuated and dominate the far zone field near the surface in cases where the waves guided by the layers decrease rapidly (as a result of the material losses) or are not supported by the structure. This should result in improved robustness, at the expense of making the method more cumbersome.

## Appendix A:

### Identities for the inversion of quasi-static and complex image terms

The quasi-static and complex image terms can be transformed by the identities<sup>44</sup>

$$\int_0^\infty \frac{e^{-jk_z b}}{jk_z} J_0(k_\rho \rho) k_\rho dk_\rho = \frac{e^{-jkr}}{r}, \quad (186)$$

$$\int_0^\infty e^{-jk_z b} J_0(k_\rho \rho) k_\rho dk_\rho = b(1 + jkr) \frac{e^{-jkr}}{r^3}, \quad (187)$$

$$\int_0^\infty jk_z e^{-jk_z b} J_0(k_\rho \rho) k_\rho dk_\rho = \left[ \left( \frac{3b^2}{r^2} - 1 \right) (1 + jkr) - k^2 b^2 \right] \frac{e^{-jkr}}{r^3}, \quad (188)$$

$$\int_0^\infty \frac{e^{-jk_z b}}{jk_z} J_0(k_\rho \rho) k_\rho^3 dk_\rho = \left[ \left( \frac{3b^2}{r^2} - 1 \right) (1 + jkr) + k^2 \rho^2 \right] \frac{e^{-jkr}}{r^3}, \quad (189)$$

$$\int_0^\infty \frac{e^{-jk_z b}}{jk_z} J_1(k_\rho \rho) dk_\rho = \frac{1}{jk_\rho} (e^{-jkb} - e^{-jkr}), \quad (190)$$

$$\int_0^\infty e^{-jk_z b} J_1(k_\rho \rho) dk_\rho = \frac{1}{\rho} \left( e^{-jkb} - \frac{b}{r} e^{-jkr} \right), \quad (191)$$

$$\int_0^\infty \frac{e^{-jk_z b}}{jk_z} J_1(k_\rho \rho) k_\rho^2 dk_\rho = \rho(1 + jkr) \frac{e^{-jkr}}{r^3}, \quad (192)$$

$$\int_0^\infty e^{-jk_z b} J_1(k_\rho \rho) k_\rho^2 dk_\rho = \left[ \frac{3b\rho}{r^2} (1 + jkr) - k^2 b\rho \right] \frac{e^{-jkr}}{r^3}, \quad (193)$$

$$\int_0^\infty \frac{e^{-jk_z b}}{jk_z} J_2(k_\rho \rho) k_\rho dk_\rho = \frac{2}{jk_\rho^2} (e^{-jkb} - e^{-jkr}) - \frac{e^{-jkr}}{r}, \quad (194)$$

$$\int_0^\infty e^{-jk_z b} J_2(k_\rho \rho) k_\rho dk_\rho = \frac{2}{\rho^2} \left( e^{-jkb} - \frac{b}{r} e^{-jkr} \right) - b(1 + jkr) \frac{e^{-jkr}}{r^3}, \quad (195)$$

$$\int_0^\infty \frac{e^{-jk_z b}}{jk_z} J_2(k_\rho \rho) k_\rho^3 dk_\rho = \left[ \frac{3\rho^2}{r^2} (1 + jkr) - k^2 \rho^2 \right] \frac{e^{-jkr}}{r^3}, \quad (196)$$

where

$$k_z = \sqrt{k^2 - k_\rho^2}, \quad r = \sqrt{\rho^2 + b^2}. \quad (197)$$

<sup>44</sup>The identity (190) is not directly used, but is included for completeness.

The first formula above is the well-known Sommerfeld identity, if  $b$  is real and positive [27, p. 66]. With some restrictions, this identity is also valid for complex-valued  $b$  [66]. The other identities can be derived (cf. [7, 67]) from (186) by integration or differentiation and by using the formulas [26, 68]

$$\int x J_0(x) dx = x J_1(x), \quad (198)$$

$$J'_0(x) = -J_1(x), \quad (199)$$

$$J_2(x) = \frac{2}{x} J_1(x) - J_0(x), \quad (200)$$

$$J_2(x) = \frac{1}{x} J_1(x) - J'_1(x). \quad (201)$$

It is important to note that the right-hand expressions in (191) and (195) have zero limits as  $\rho \rightarrow 0$  with finite  $b$ , but are singular in this limit if  $b = 0$ .

## Appendix B: Identities for the inversion of pole terms

The pole terms can be transformed by the identities

$$\int_0^\infty J_0(k_\rho \rho) \frac{2k_{\rho i}^2 k_\rho dk_\rho}{k_\rho^4 - k_{\rho i}^4} = - \left[ \frac{j\pi}{2} H_0^{(2)}(k_{\rho i} \rho) + K_0(k_{\rho i} \rho) \right], \quad (202)$$

$$\int_0^\infty J_1(k_\rho \rho) \frac{2k_{\rho i}^3 dk_\rho}{k_\rho^4 - k_{\rho i}^4} = - \left[ \frac{j\pi}{2} H_1^{(2)}(k_{\rho i} \rho) - K_1(k_{\rho i} \rho) + \frac{2}{k_{\rho i} \rho} \right], \quad (203)$$

$$\int_0^\infty J_1(k_\rho \rho) \frac{2k_{\rho i} k_\rho^2 dk_\rho}{k_\rho^4 - k_{\rho i}^4} = - \left[ \frac{j\pi}{2} H_1^{(2)}(k_{\rho i} \rho) + K_1(k_{\rho i} \rho) \right], \quad (204)$$

$$\int_0^\infty J_2(k_\rho \rho) \frac{2k_{\rho i}^2 k_\rho dk_\rho}{k_\rho^4 - k_{\rho i}^4} = - \left[ \frac{j\pi}{2} H_2^{(2)}(k_{\rho i} \rho) - K_2(k_{\rho i} \rho) + \frac{4}{(k_{\rho i} \rho)^2} \right], \quad (205)$$

where  $K_n$  is the modified Bessel function of order  $n$ , which is related to the Hankel function as [26]

$$H_n^{(2)}(-jx) = \frac{2j^{n+1}}{\pi} K_n(x). \quad (206)$$

These identities can be derived by using (88)–(89), contour deformation, and the residue theorem [69, p. 294].

It is important to note that the right-hand expressions in (202)–(205) are bounded for  $\rho \rightarrow 0$ , as can be seen by utilizing the small-argument forms [26]

$$H_0^{(2)}(x) \xrightarrow{x \rightarrow 0} -\frac{2j}{\pi} \ln x, \quad H_n^{(2)}(x) \xrightarrow{x \rightarrow 0} \frac{j}{\pi} \left( \frac{2}{x} \right)^n, \quad n = 1, 2, \quad (207)$$

$$K_0(x) \xrightarrow{x \rightarrow 0} -\ln x, \quad K_n(x) \xrightarrow{x \rightarrow 0} \frac{1}{2} \left( \frac{2}{x} \right)^n, \quad n = 1, 2. \quad (208)$$

## References

- [1] K. A. Michalski, "Extrapolation methods for Sommerfeld integral tails (Invited review paper)," *IEEE Trans. Antennas Propagat.*, vol. 46, pp. 1405–1418, Oct. 1998.
- [2] M. Tsai, C. Chen, and N. G. Alexopoulos, "Sommerfeld integrals in modeling interconnects and microstrip elements in multi-layered media," *Electromagn.*, vol. 18, pp. 267–288, 1998.
- [3] D. G. Fang, J. J. Yang, and G. Y. Delisle, "Discrete image theory for horizontal electric dipoles in a multilayered medium," *IEE Proc., Pt. H*, vol. 135, pp. 297–303, Oct. 1988.
- [4] Y. L. Chow, J. J. Yang, D. G. Fang, and G. E. Howard, "A closed-form spatial Green's function for the thick microstrip substrate," *IEEE Trans. Microwave Theory Tech.*, vol. 39, pp. 588–592, Mar. 1991.
- [5] F. Ling and J. Jin, "Discrete complex image method for Green's functions of general multi-layer media," *IEEE Microwave Guided Wave Lett.*, vol. 10, pp. 400–402, Oct. 2000.
- [6] P. Ylä-Oijala, M. Taskinen, and J. Sarvas, "Multilayered media Green's functions for MPIE with general electric and magnetic sources by the Hertz potential approach," in *Progress in Electromagnetics Research* (J. A. Kong, ed.), vol. PIER 33, pp. 141–165, Cambridge, MA: EMW Publ., 2001.
- [7] P. Ylä-Oijala and M. Taskinen, "Efficient formulation of closed-form Green's functions for general electric and magnetic sources in multilayered media," *IEEE Trans. Antennas Propagat.*, vol. 51, pp. 2106–2115, Aug. 2003.
- [8] X. He, S. Gong, and Q. Liu, "Fast computation of spatial Green's functions of multilayered microstrip antennas," *Microwave & Opt. Technol. Lett.*, vol. 45, no. 1, pp. 85–88, 2005.
- [9] M. Yuan, T. K. Sarkar, and M. Salazar-Palma, "A direct discrete complex image method from the closed-form Green's functions in multilayered media," *IEEE Trans. Microwave Theory Tech.*, vol. 54, pp. 1025–1032, Mar. 2006.
- [10] F. Ling, V. Okhmatovski, B. Song, and A. Dengi, "Systematic extraction of static images from layered media Green's function for accurate DCIM implementation," *IEEE Antennas Wireless Propagat. Lett.*, vol. 6, pp. 215–218, 2007.
- [11] M. Zhang, L. Li, and Y. Tian, "An efficient approach for extracting poles of Green's functions in general multilayered media," *IEEE Trans. Antennas Propagat.*, vol. 56, pp. 269–273, Jan. 2008.
- [12] K. A. Michalski, "The mixed-potential electric field integral equation for objects in layered media," *Arch. Elek. Übertragung.*, vol. 39, pp. 317–322, Sept.–Oct. 1985.
- [13] J. R. Mosig, "Arbitrarily shaped microstrip structures and their analysis with a mixed potential integral equation," *IEEE Trans. Microwave Theory Tech.*, vol. 36, pp. 314–323, Feb. 1988.



- [14] K. A. Michalski and D. Zheng, "Electromagnetic scattering and radiation by surfaces of arbitrary shape in layered media, Part I: Theory," *IEEE Trans. Antennas Propagat.*, vol. 38, pp. 335–344, Mar. 1990.
- [15] K. A. Michalski and J. R. Mosig, "Multilayered media Green's functions in integral equation formulations (Invited review paper)," *IEEE Trans. Antennas Propagat.*, vol. 45, pp. 508–519, Mar. 1997.
- [16] N. N. Feng, D. G. Fang, and W. P. Huang, "Full wave discrete images of an electric dipole for uniaxial substrate," in *Proc. Int. Conf. on Microwave and Millimeter Wave Technology*, (Beijing, China), pp. 998–1001, July 1998.
- [17] K. A. Michalski, "Formulation of mixed-potential integral equations for arbitrarily shaped microstrip structures with uniaxial substrates," *J. Electromagn. Waves Appl.*, vol. 7, no. 7, pp. 899–917, 1993.
- [18] K. A. Michalski, "Electromagnetic field computation in planar multilayers," in *Encyclopedia of RF and Microwave Engineering* (K. Chang, ed.), vol. 2, pp. 1163–1190, Wiley-Interscience, 2005.
- [19] D. R. Wilton, "Review of current status and trends in the use of integral equations in computational electromagnetics," *Electromagn.*, vol. 12, pp. 287–341, July-Dec. 1992.
- [20] D. R. Wilton, "Computational methods," in *Scattering. Scattering and Inverse Scattering in Pure and Applied Science* (R. Pike and P. Sabatier, eds.), ch. 1.5.5, pp. 316–365, London: Academic Press, 2002.
- [21] L. B. Felsen and N. Marcuvitz, *Radiation and Scattering of Waves*. Englewood Cliffs, N.J.: Prentice Hall, 1973.
- [22] C.-I. G. Hsu, R. F. Harrington, K. A. Michalski, and D. Zheng, "Analysis of a multiconductor transmission lines of arbitrary cross-section in multilayered uniaxial media," *IEEE Trans. Microwave Theory Tech.*, vol. 41, pp. 70–78, Jan. 1993.
- [23] L. M. Delves and J. N. Lyness, "A numerical method for locating the zeros of an analytic function," *Math. Comput.*, vol. 21, pp. 543–560, Oct. 1967.
- [24] R. Rodriguez-Berral, F. Mesa, and F. Medina, "Systematic and efficient root finder for computing the modal spectrum of planar layered waveguides," *Int. J. RF Microwave Computer-Aided Eng.*, vol. 14, pp. 73–83, Jan. 2004.
- [25] M. Metcalf and J. Reid, *FORTTRAN 90/95 explained*. Oxford, UK: Oxford University Press, 1996.
- [26] M. Abramowitz and I. A. Stegun, eds., *Handbook of Mathematical Functions*. New York: Dover, 1965.
- [27] W. C. Chew, *Waves and Fields in Inhomogeneous Media*. New York: IEEE Press, 1995.

- [28] M. Paulus, P. Gay-Balmaz, and O. J. F. Martin, "Accurate and efficient computation of the Green's tensor for stratified media," *Phys. Rev. E*, vol. 62, pp. 5797–5807, Oct. 2000.
- [29] T. Yu and W. Cai, "FIFA – Fast Interpolation and Filtering Algorithm for calculating dyadic Green's function in the electromagnetic scattering of multi-layered structures," *Commun. Computat. Phys.*, vol. 1, pp. 229–260, Apr. 2006.
- [30] M. Yuan and T. K. Sarkar, "Computation of the Sommerfeld integral tails using the Matrix Pencil Method," *IEEE Trans. Antennas Propagat.*, vol. 54, pp. 1358–1362, Apr. 2006.
- [31] G. Evans, *Practical Numerical Integration*. New York: Wiley, 1993.
- [32] J. R. Mosig, "Integral equation technique," in *Numerical Techniques for Microwave and Millimeter-Wave Passive Structures* (T. Itoh, ed.), pp. 133–213, New York: Wiley, 1989.
- [33] J. R. Mosig and A. A. Melecón, "Green's functions in lossy layered media: integration along the imaginary axis and asymptotic behavior," *IEEE Trans. Antennas Propagat.*, vol. 51, pp. 3200–3208, Dec. 2003.
- [34] N. V. Shuley, R. R. Boix, F. Medina, and M. Horno, "On the fast approximation of Green's functions in MPIE formulations for planar layered media," *IEEE Trans. Microwave Theory Tech.*, vol. 50, pp. 2185–2192, Sept. 2002.
- [35] P. Cornille, "Numerical saddle point method," *J. Math. Anal. Appl.*, vol. 38, pp. 633–639, 1972.
- [36] K. A. Michalski, "On the efficient evaluation of integrals arising in the Sommerfeld halfspace problem," in *Moment Methods in Antennas and Scatterers* (R. C. Hansen, ed.), pp. 325–331, Boston: Artech House, 1990.
- [37] T. J. Cui and W. C. Chew, "Fast evaluation of Sommerfeld integrals for EM scattering and radiation by three-dimensional buried objects," *IEEE Trans. Geosci. Remote Sens.*, vol. 37, pp. 887–900, Mar. 1999.
- [38] J. J. Yang, Y. L. Chow, and D. G. Fang, "Discrete complex images of a three-dimensional dipole above and within a lossy ground," *IEE Proc., Pt. H*, vol. 138, pp. 319–326, Aug. 1991.
- [39] K. A. Michalski and J. R. Mosig, "Discrete complex image mixed-potential integral equation analysis of microstrip patch antennas with vertical probe feeds (Invited paper)," *Electromagn.*, vol. 15, pp. 377–392, July-Aug. 1995.
- [40] M. I. Aksun, "A robust approach for the derivation of closed-form Green's functions," *IEEE Trans. Microwave Theory Tech.*, vol. 44, pp. 651–658, May 1996.
- [41] M. I. Aksun and G. Dural, "Clarification of issues on the closed-form Green's functions in stratified media," *IEEE Trans. Antennas Propagat.*, vol. 53, pp. 3644–3653, Nov. 2005.
- [42] L. Zhuang, G. Zhu, Y. Zhang, and B. Xiao, "An improved discrete complex image method for Green's functions in layered media," *Microwave & Opt. Technol. Lett.*, vol. 49, no. 6, pp. 1337–1340, 2007.

- [43] T. H. Cormen, C. E. Leiserson, R. L. Rivest, and C. Stein, *Introduction to Algorithms*. Cambridge, Mass.: MIT Press, 2nd ed., 2001.
- [44] K. A. Michalski, "Automatic, robust and efficient pole location for planar, uniaxial multilayers." Technical Report for Alpha Omega Electromagnetics, June 2006.
- [45] E. Anemogiannis and E. N. Glytsis, "Multilayer waveguides: Efficient numerical analysis of general structures," *J. Lightwave Technol.*, vol. 10, pp. 1344–1351, Oct. 1992.
- [46] R. E. Smith, G. W. Forbes, and S. N. Houde-Walter, "Unfolding the multivalued planar waveguide dispersion relation," *IEEE J. Quantum Electron.*, vol. 29, pp. 1031–1034, Apr. 1993.
- [47] R. E. Smith and S. N. Houde-Walter, "The migration of bound and leaky solutions to the waveguide dispersion relation," *J. Lightwave Technol.*, vol. 11, pp. 1760–1768, Nov. 1993.
- [48] A. Bakhtazad, H. Abiri, and R. Ghayour, "A general transform for regularizing planar open waveguide dispersion relation," *J. Lightwave Technol.*, vol. 15, pp. 383–390, Feb. 1997.
- [49] R. Rodriguez-Berral, F. Mesa, and F. Medina, "Appropriate formulation of the characteristic equation for open nonreciprocal layered waveguides with different upper and lower half-spaces," *IEEE Trans. Microwave Theory Tech.*, vol. 53, pp. 1613–1623, May 2005.
- [50] F. J. Demuynek, G. A. E. Vandenbosch, and A. R. van de Capelle, "The expansion wave concept—Part I: Efficient calculation of spatial Green's functions in a stratified dielectric medium," *IEEE Trans. Antennas Propagat.*, vol. 46, pp. 397–406, Mar. 1998.
- [51] A. K. Abdelmageed and A. A. K. Mohsen, "An accurate computation of Green's functions for multilayered media in the near-field region," *Microwave & Opt. Technol. Lett.*, vol. 29, no. 2, pp. 130–131, 2001.
- [52] N. Hojjat, S. Safavi-Naeini, and Y. L. Chow, "Numerical computation of complex image Green's functions for multilayered dielectric media: near-field zone and the interface region," *IEE Proc.-Microw. Antennas Propagat.*, vol. 145, pp. 449–454, Dec. 1998.
- [53] S. Teo, S. Chew, and M. Leong, "Error analysis of the discrete complex image method and pole extraction," *IEEE Trans. Microwave Theory Tech.*, vol. 51, pp. 406–413, Feb. 2003.
- [54] A. Ishimaru, *Electromagnetic Wave Propagation, Radiation, and Scattering*. Englewood Cliffs, NJ: Prentice Hall, 1991.
- [55] G. Tyras, *Radiation and Propagation of Electromagnetic Waves*. New York: Academic Press, 1969.
- [56] P. Baccarelli, P. Burghignoni, F. Frezza, A. Galli, G. Lovat, and D. R. Jackson, "Uniform analytical representation of the continuous spectrum excited by dipole sources in a multi-layer dielectric structure through weighted cylindrical leaky waves," *IEEE Trans. Antennas Propagat.*, vol. 52, pp. 653–664, Mar. 2004.

- [57] R. R. Boix, F. Mesa, and F. Medina, "Derivation of closed-form Green's functions for multi-layered media via the method of total least squares." to be published, 2007.
- [58] R. R. Boix, F. Mesa, and F. Medina, "Application of total least squares to the derivation of closed-form Green's functions for planar layered media," *IEEE Trans. Microwave Theory Tech.*, vol. 55, pp. 268–280, Feb. 2007.
- [59] L. M. Brekhovskikh, *Waves in Layered Media*. New York: Academic Press, 2nd ed., 1980.
- [60] G. D. Bernard and A. Ishimaru, "On complex waves," *Proc. IEE*, vol. 114, pp. 43–49, Jan. 1967.
- [61] G. N. Watson, *A Treatise on the Theory of Bessel Functions*. New York: Cambridge University Press, 1995.
- [62] T. K. Sarkar and O. Pereira, "Using the matrix pencil method to estimate the parameters of a sum of complex exponentials," *IEEE Antennas Propagat. Magaz.*, vol. 37, pp. 48–55, Feb. 1995.
- [63] R. S. Adve, T. K. Sarkar, O. M. C. Pereira-Filho, and S. M. Rao, "Extrapolation of time-domain responses from three-dimensional conducting objects utilizing the matrix pencil technique," *IEEE Trans. Antennas Propagat.*, vol. 45, pp. 147–156, Jan. 1997.
- [64] N. Kınayman and M. I. Aksun, "Efficient use of closed-form Green's functions for the analysis of planar geometries with vertical connections," *IEEE Trans. Microwave Theory Tech.*, vol. 45, pp. 593–603, Apr. 1997.
- [65] F. Ling, J. Liu, and J. Jin, "Efficient electromagnetic modeling of three-dimensional multi-layer microstrip antennas and circuits," *IEEE Trans. Antennas Propagat.*, vol. 50, pp. 1628–1635, June 2002.
- [66] Y. L. Li and M. J. White, "Near-field computation for sound propagation above ground—Using complex image theory," *J. Acoust. Soc. Am.*, vol. 99, pp. 755–760, Feb. 1996.
- [67] P. C. Clemmow, "The resolution of a dipole field into transverse electric and transverse magnetic waves," *Proc. IEE*, vol. 110, pp. 107–111, Jan. 1963.
- [68] I. S. Gradshteyn and I. M. Ryzhik, eds., *Table of Integrals, Series, and Products*. New York: Academic Press, 7th ed., 2007.
- [69] J. A. Kong, *Electromagnetic Wave Theory*. New York: Wiley, 2nd ed., 1990.